END

DATE
FILMED

2-77

1.0

2.8   2.5
3.2   2.2
3.6
4.0   2.0

1.1

1.8

1.25   1.4   1.6

MICROCOPY RESOLUTION TEST CHART
NATIONAL BUREAU OF STANDARDS-1963

MASSACHUSETTS INSTITUTE OF TECHNOLOGY

LINCOLN LABORATORY

SOLID STATE RESEARCH

QUARTERLY TECHNICAL SUMMARY REPORT

1 MAY – 31 JULY 1976

ISSUED 26 OCTOBER 1976

D D C

RECEIVED
JAN 21 1977

D
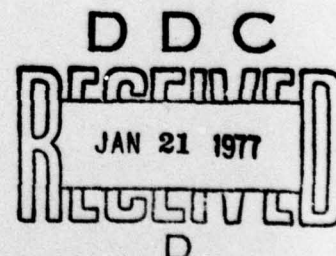
LEXINGTON   MASSACHUSETTS

ABSTRACT

This report covers in detail the solid state research work of the Solid State Division at Lincoln Laboratory for the period 1 May through 31 July 1976. The topics covered are Solid State Device Research, Quantum Electronics, Materials Research, Microelectronics, and Surface Wave Technology. Funding is primarily provided by the Air Force, with additional support provided by the Army (BMDATC), ARPA (MSO, IPTO), NSF, and ERDA.

CONTENTS

INTRODUCTION

I. SOLID STATE DEVICE RESEARCH

A GaAs $p^+n^-n^+$ directional-coupler switch which is operable both as a passive coupler with 98-percent power transfer and as an optical switch has been developed. The switch is characterized by 17-dB power isolation and by constant total power output (within 0.2 dB) throughout the switching-bias range.

HgCdTe photodiodes have been characterized at high frequency for use as gigahertz-response CO_2 laser heterodyne receivers. In order to evaluate device uniformity and sensitivity, the following measurements were carried out: pulse response vs frequency, high-frequency raster scan profiles, RF noise output as a function of detector bias and frequency, direct heterodyne detection, and blackbody heterodyne radiometry. These measurements show that it is necessary to use high-frequency characterization to get an accurate picture of the high-frequency performance of these devices, and that low-frequency measurements can give misleading results.

A temperature-gradient liquid-phase epitaxial growth apparatus $Pb_{1-x}Sn_xTe$ has been constructed and utilized. For the growth of $Pb_{1-x}Sn_xTe$ films on PbTe substrates, the imposed temperature gradient (a) does not improve the film quality of heteroepitaxial growths in the $Pb_{1-x}Sn_xTe$ system, and (b) does not have a measurable effect on the Sn/Pb ratio of the grown film.

II. QUANTUM ELECTRONICS

Low-threshold, CW lasing has been obtained in $NdNa_5(WO_4)_4$, $K_3Nd(PO_4)_2$, and $Na_3Nd(PO_4)_2$. Laser thresholds and efficiencies are given for these new compounds, together with fluorescent lifetimes, as a function of Nd concentration for crystals in which Nd is replaced by La.

Substantial narrowing of the Doppler width of molecular absorption lines has been observed in an effusive molecular beam from a capillary array nozzle using broadly tunable diode lasers. Hitherto unresolved Λ-doublet splittings in the $^2\pi_{3/2}$ electronic ground state of NO have been studied.

The performance of the vibrational energy transfer lasers optically pumped by doubled CO_2 radiation has been improved. Slope efficiencies close to unit quantum efficiency and output energies up to 13 mJ have been demonstrated for the CO-CO_2 system. Laser action has been observed on a new transition in CS_2; by pumping the 10^01 level directly, operation was obtained on the $10^01 \rightarrow 10^00$ transition at 6.6 μm.

Considerable progress has been made in the HBr-pumped 16-μm CO_2 laser. The pulse energy has been scaled to 120 μJ. In order to demonstrate that the

16-μm laser can be made stepwise tunable, laser action in the $^{13}C^{16}O_2$ isotopic series has been obtained. The threshold for the 9.6-μm stimulating pulse has been measured to be ~3 mJ, indicating that a rather large but conventional sealed-off Q-switched laser would be sufficient for driving an isotopic 16-μm laser. Kinetic measurements of the relaxation of the 16-μm lower level indicate that its relaxation time is of the order of 10^{-5} sec at typical pressures. As a result, high-repetition-rate operation of the laser is possible.

Experimental work on the quantum electronics of cryogenic liquids has progressed along three avenues: (a) measurement of the vibrational kinetics of molecules in liquid solutions, (b) observation of laser-induced photochemistry in several liquid hosts, and (c) measurement of the infrared spectra of various dopant molecules. The results indicate that laser photochemistry in liquid media could have practical applications.

III. MATERIAL RESEARCH

In order to obtain a better understanding of the mechanism of the photoelectrolysis of water in cells with TiO_2 anodes, the interaction of absorbed H_2O molecules with TiO_2 surfaces is being investigated by ultraviolet photoemission spectroscopy. Comparison of the spectra for Ar-bombarded TiO_2 before and after exposure to water vapor indicates that the H_2O molecules form bonds to the oxygen vacancies produced by bombardment.

The effect of cesiation on the work function of CdTe is being studied in order to determine the possibility of producing negative-electron-affinity CdTe surfaces that can be used to make transferred-electron photocathodes with a graded-gap $Hg_xCd_{1-x}Te$ structure. In initial experiments, a reduction of 2.4 eV in the work function of both n- and p-type CdTe has been obtained by a series of alternate exposures to Cs and O_2.

A preliminary study has been undertaken to assess the potential of insulator-metal transitions for utilization in optical switching devices such as modulators and switchable diffraction gratings for use as variable-wavelength filters. Modulation at 151 μm and 337 μm has been achieved with devices employing thermally switched VO_2 films deposited by reactive sputtering on sapphire substrates.

IV. MICROELECTRONICS

Considerable attention has been given to the problem of improving yields in CCD processing. Wafers of 30- × 30-cell prototype imaging arrays have been fabricated with improved processing techniques, and have exhibited yields of over 90 percent when tested for diode leakage and gate-to-gate and gate-to-substrate shorts. Dynamic testing of these devices will result in a somewhat lower yield, but the results of static testing are very encouraging.

Several 30- × 30-cell prototype imaging arrays have been dynamically tested using an electrical input signal. The capability of inserting signals electrically is a useful addition to a CCD imaging device, and costs little in terms of added device area. Electrical inputs are simpler and more effective than optical inputs in setting clocking voltages for optimum operation and for measuring charge transfer efficiency. Transfer efficiencies of 0.9998 or greater have been measured for the output registers of several devices, and the transfer efficiency for a single complete device has been determined to be equivalently high.

Impurities have been gettered from semi-insulating gallium arsenide using silicon- and neon-ion-implantation damage and a subsequent 16-hr anneal at 750°C. The amount of gettering was determined by an evaluation of epitaxial layers grown on the gettered samples after removal of the damaged material. Impurity profiles of layers grown on these surfaces show a dramatic reduction in the outdiffusion of compensating impurities from the substrate into the epitaxial layer. It is possible that this ion-implantation-damage gettering will be useful in providing better substrates for application to gallium arsenide microwave FETs. In addition, because the gettering effects occur in the temperature range for epitaxial growth and ion-implantation anneals, this gettering phenomenon could also be important in understanding and improving growth and annealing procedures.

V. SURFACE-WAVE TECHNOLOGY

The use of Cu_L radiation for x-ray lithography has been demonstrated. For replicating patterns with linewidths of the order of 1000 Å, it is preferable to use softer x-ray radiation than that obtained from the commonly employed aluminum targets. The use of the characteristic L radiation (13.3 Å) emitted from a copper target increases the attenuation in the mask absorber pattern and reduces the range of randomly directed Auger and photoelectrons that are excited when the exposing x-ray is absorbed. Because of the high absorption at longer wavelengths, special x-ray masks with thin low-absorption membranes were employed.

A second generation of pulse expanders and compressors has been developed for the MASR (Multiple-Antenna Surveillance Radar) system. These reflective-array devices generate and compress linear-FM waveforms with a duration of 150 μsec, bandwidth of 10 MHz, and time-bandwidth product of 1500. The use of bismuth-germanium-oxide (BGO) substrates allowed 150 μsec of dispersion to be obtained in a relatively compact device. Because of the large time-bandwidth product, it was necessary that the pulse expanders have especially low loss. By careful design of the transducers and reflection gratings, overall CW insertion loss for the expanders was held to 30 dB. This provided 60 dB of signal to noise in the expanded waveform. A complete subsystem containing six dispersive lines has been assembled for the MASR system.

A dual acoustoelectric convolver for decoding differential-phase-shift-keyed (DPSK) data has been developed for the ARPA Packet Radio System. This device decodes DPSK data which have been spread to a 100-MHz bandwidth by means of continuously changing pseudorandom, bit-encoding waveforms. The bit rate is 100 kbps. DPSK decoding is provided by splitting a standard convolver structure into two segments and comparing the phase of the signal from the two segments in a sum-difference hybrid. Improved packaging techniques provide temperature stability and are compatible with commercial fabrication procedures.

REPORTS ON SOLID STATE RESEARCH

15 May through 15 August 1976

PUBLISHED REPORTS

Journal Articles

JA No.

4469A	Low-Threshold Transversely Excited NdP_5O_{14} Laser	S. R. Chinn J. W. Pierce H. Heckscher	Appl. Opt. <u>15</u>, 1444 (1976)
4539	Interpretation of Infrared Modulation Spectroscopy Data in Graphite by the Slonczewski-Weiss-McClure Band Model	M. S. Dresselhaus* G. Dresselhaus	Phys. Rev. B <u>13</u>, 4635 (1976)
4544	Threshold Ambiguities in Absorptive Laser Damage to Dielectric Films	R. H. Picard* D. Milam* R. A. Bradbury* J. C. C. Fan	Chapter in <u>Laser Induced Damage in Optical Materials</u> (NBS Special Publication, 1976), p. 272, Proc. 7th Symp. on Damage to Laser Materials, Boulder, Colorado, 29-31 July 1975
4570	Thermal Faceting of (110) and (111) Surfaces of MgO	V. E. Henrich	Surf. Sci. <u>57</u>, 385 (1976)
4572	Crystal Structure and Fluorescence Lifetime of Potassium Neodymium Orthophosphate, $K_3Nd(PO_4)_2$, a New Laser Material	H. Y-P. Hong S. R. Chinn	Mater. Res. Bull. <u>11</u>, 421 (1976), DDC AD-A026811
4573	Acoustoelectric Convolvers for Programmable Matched Filtering in Spread-Spectrum Systems	J. H. Cafarella W. M. Brown, Jr. E. Stern J. A. Alusow	Proc. IEEE <u>64</u>, 756 (1976)
4574	The Schottky Diode Acoustoelectric Memory and Correlator — A Novel Programmable Signal Processor	K. A. Ingebrigtsen	Proc. IEEE <u>64</u>, 764 (1976), DDC AD-A028456
4576	Vibrational Energy Relaxation in Liquid N_2–CO Mixtures	S. R. J. Brueck R. M. Osgood, Jr.	Chem. Phys. Lett. <u>39</u>, 568 (1976), DDC AD-A028459
4581	Surface-Acoustic-Wave Resonators	D. T. Bell* R. C. M. Li	Proc. IEEE <u>64</u>, 711 (1976), DDC AD-A028460
4583	Properties and Applications of Reflective-Array Devices	R. C. Williamson	Proc. IEEE <u>64</u>, 702 (1976), DDC AD-A028461

---

*Author not at Lincoln Laboratory.

*Author not at Lincoln Laboratory.

*   *   *   *   *

UNPUBLISHED REPORTS

Journal Articles

_____

* Author not at Lincoln Laboratory.

*Titles of Meeting Speeches are listed for information only. No copies are available for distribution.

*Author not at Lincoln Laboratory.

---

[*] Author not at Lincoln Laboratory.

ORGANIZATION

SOLID STATE DIVISION

A. L. McWhorter, *Head*
I. Melngailis, *Associate Head*
C. R. Grant, *Assistant*

P. E. Tannenwald

QUANTUM ELECTRONICS

A. Mooradian, *Leader*
P. L. Kelley, *Associate Leader*

Barch, W. E.	Heckscher, H.
Brueck, S. R. J.	Kildal, H.
Burke, J. W.	Larsen, D. M.
Chinn, S. R.	Menyuk, N.
DeFeo, W. E.	Moulton, P. F.
Deutsch, T. F.	Osgood, R. M.
Fetterman, H. R.	Parker, C. D.
Hancock, R. C.	Pine, A. S.

ELECTRONIC MATERIALS

A. J. Strauss, *Leader*
H. J. Zeiger, *Associate Leader*

Anderson, C. H., Jr.	Krohn, L., Jr.
Animalu, A. O. E.	LaFleur, W. J.
Button, M. J.	Mastromattei, E. L.
Delaney, E. J.	Mavroides, J. G.
Dresselhaus, G.	Mroczkowski, I. H.
Dwight, K., Jr.	Oli, B.*
Fahey, R. E.	Owens, E. B.
Fan, J. C. C.	Palm, B. J.
Feldman, B.	Pantano, J. V.
Finn, M. C.	Pierce, J. W.
Henrich, V. E.	Plonko, M. C.
Hong, H. Y-P.	Reed, T. B.
Hsieh, J. J.	Tchernev, D. I.
Iseler, G. W.	Tracy, D. M.
Kafalas, J. A.	Vohl, P.
Kolesar, D. F.	Zavracky, P. M.

APPLIED PHYSICS

A. G. Foyt, *Leader*
T. C. Harman, *Assistant Leader*
C. E. Hurwitz, *Assistant Leader*

Belanger, L. J.	Lind, T. A.
Calawa, A. R.	McBride, W. F.
Carter, F. B.	Orphanos, W. G.
DeMeo, N. L., Jr.	Paladino, A. E.
Donnelly, J. P.	Rossi, J. A.
Ferrante, G. A.	Spears, D. L.
Groves, S. H.	Tsang, D.*
Leonberger, F. J.	Walpole, J. N.

SURFACE WAVE TECHNOLOGY

E. Stern, *Leader*
R. C. Williamson, *Assistant Leader*

Brogan, W. T.	Li, R. C. M.
Cafarella, J. H.	Melngailis, J.
DeGraff, P. D.	Ralston, R. W.
Dolat, V. S.	Reible, S. A.
Efremow, N., Jr.	Smith, H. I.
Flanders, D. C.*	Vlannes, N.*
Kernan, W. C.	

MICROELECTRONICS

W. T. Lindley, *Leader*
F. J. Bachner, *Assistant Leader*

Beatrice, P. A.	Gray, R. V.
Bozler, C. O.	Lincoln, G. A., Jr.
Burke, B. E.	McGonagle, W. H.
Clifton, B. J.	Mountain, R. W.
Clough, T. F.	Murphy, R. A.
Cohen, R. A.	Pichler, H. H.
Durant, G. L.	Smythe, D. L., Jr.
Foley, G. H.	Wilde, R. E.
Grant, L. L.	

---

* Research assistant

I. SOLID STATE DEVICE RESEARCH

A. GaAs $p^+n^-n^+$ DIRECTIONAL-COUPLER SWITCH

A waveguide switch is a fundamental component necessary for the development of GaAs-based integrated optical circuits. We report here the successful development of a GaAs $p^+n^-n^+$ directional-coupler switch operable both as a passive coupler with 98-percent power transfer and as an optical switch. The switch is characterized by 17-dB power isolation in both the switched and unswitched state and by constant total power output (within 0.2 dB) throughout the switching-bias range. This switch performance was found to depend on the crystallographic direction chosen for light propagation. The device was fabricated from a pair of closely spaced low-loss ($\alpha \sim 1$ cm^{-1} at 1.06 μm), single-mode $p^+n^-n^+$ channel-stop strip guides.[1,2] The switching is achieved using a scheme proposed several years ago in which the phase synchronism of the coupler guides is destroyed via the electro-optic effect.[3-5] Initial devices in GaAs based on this scheme used planar films.[6] A GaAs switch using metal-gap strip guides also has been reported;[7] however, this device had only about 75-percent power transfer and there was significant power loss at switching biases.
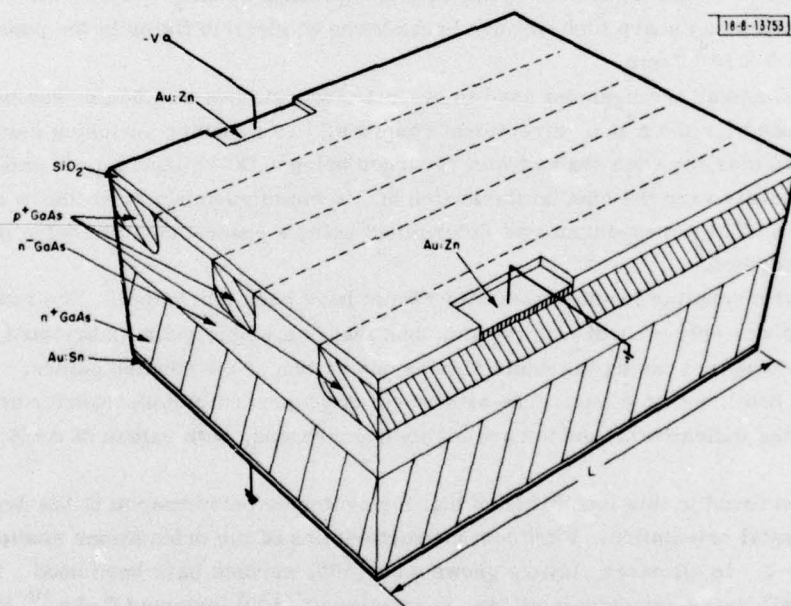
Fig. I-1. Cross-section sketch of GaAs $p^+n^-n^+$ directional-coupler switch. Light is guided in the two channels between the three p^+ regions. Electro-optic switching is achieved by reverse-biasing one of the outer p^+n^- junctions as shown. The coupling length is that of the device length, L.

A cross-section sketch of a $p^+n^-n^+$ directional-coupler switch is shown in Fig. I-1. The device has a planar structure and is composed of an n^+ substrate, an n^- guiding layer, and three p^+ regions: two that lie along the outside edges of the guiding channels and one that lies in the space between the guides. These p^+ regions reduce the effective guide index outside the channels where the light propagates, and thus serve as optical-channel stops. The guides are

1

highly synchronous and the device length is one coupling length, L, so that maximum power transfer to the coupled guide could be obtained at zero bias. The optical switching was achieved by reverse-biasing the p^+n^- junction along the outside edge of one of the channels. The applied electric field alters the propagation constant of the coupled guide relative to the input guide through the electro-optic effect. This reduces the coupling length and the fraction of power transferred. To achieve optimum switching, the applied bias was adjusted to obtain maximum power output from the input guide.

The n^- guiding layer had a concentration in the mid-10^{14} cm^{-3} range and was grown by vapor-phase epitaxy on a 1×10^{18} cm^{-3} n^+ substrate. The p^+ regions were formed by a multiple-energy Be$^+$ ion implantation[8] and have a uniform concentration of $\sim 3 \times 10^{18}$ cm^{-3} to a depth of 1.5 μm with a junction 2 μm from the surface. For the implantations, a Si$_3$N$_4$-encapsulation technique[9] was used. Samples were implanted through a thick photoresist mask with doses of 2.5×10^{14} cm^{-2} at 400 keV, 2×10^{14} cm^{-2} at 220 keV, and 2×10^{14} cm^{-2} at 100 keV. A 15-min. 900°C anneal was used to activate the Be. Further details of the above fabrication procedures are given in Refs. 1, 2, 8, and 9. Following the anneal, the nitride layer was removed and the sample was coated with 3000 Å of pyrolytic SiO$_2$ at 400°C. A large-area back contact of Au:Sn was then plated. Contacts to the outside p^+ regions (which were 3 mils wide) were formed by plating Au:Zn through etched openings in SiO$_2$ and then microalloying. The p^+n^- junctions had sharp high-voltage breakdowns at electric fields in the punched-through n^- layer of $\sim 1.5 \times 10^5$ V/cm.

The experimental arrangement used to evaluate the switches at 1.06 μm was basically the same as that used for the $p^+n^-n^+$ directional couplers.[2] To measure switching performance, power output vs bias for each channel was recorded using a DC voltage source and potentiometer to continuously vary the bias on the switch and to simultaneously drive the x axis of a chart recorder. The power output was determined using a phase-sensitive detection scheme previously described.[2]

Devices with coupling lengths from 4 to 14 mm have been fabricated.[2] The attenuation of these couplers was only ~ 0.1 dB/cm greater than that of a single guide (fabricated on the same wafer with the coupler) having the same dimensions as one of the coupled guides. Switches reported here had L $\simeq$ 7 to 8 mm. The attainment of 98-percent power transfer at zero bias for these lengths indicates the guides are highly synchronous, with values of $\Delta\beta/\beta \lesssim 3 \times 10^{-6}$ (Ref. 2).

It has been found in this investigation that the switching performance of the devices is a function of crystal orientation. Pertinent characteristics of the orientations studied are detailed in Fig. I-2. In all cases, layers grown on a {100} surface have been used. Figure I-2(a) reviews the well-known anisotropic etching properties of {100}-oriented GaAs.[10] When square mesas with sides parallel to cleavage directions are etched in a Br-Ch$_3$OH solution, two parallel sides etch outward, appearing as shaded areas in a top view and giving the trapezoidal profile shown here. The sloped sides are A{111} planes, and the [111] direction is chosen as an outward normal.[11] The other two parallel sides etch inward, yielding the profile illustrated to the right. From the defined A face, the [011] and [0$\bar{1}$1] directions can be determined as shown.

Using this coordinate system, the electro-optic effect in GaAs (Ref. 12) is illustrated in Fig. I-2(b). For a DC electric field E in the [100] direction, corresponding to a reverse bias of the p^+n^- junction, the index increases along the [011] direction and decreases along the [0$\bar{1}$1] direction by an amount (3.2×10^{-4}) E, where E is in units of 10^5 V/cm. Thus, a TE wave
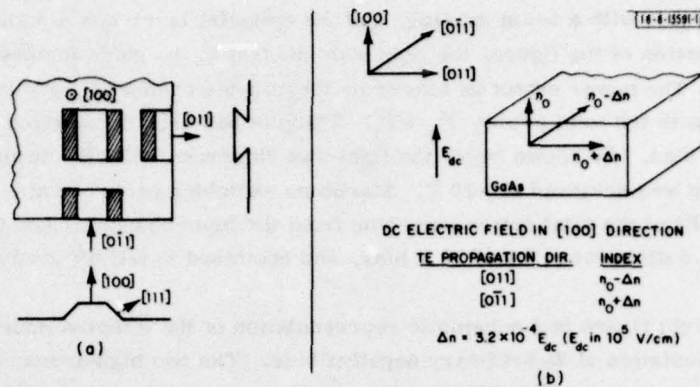
Fig. I-2(a). Diagram illustrating anisotropic etching of square mesas on {100} GaAs surface using Br-CH₃OH etching solution. (b) Diagram illustrating the electro-optic effect for the directions defined in (a). The DC electric field direction corresponds to that for reverse-biasing the p^+n^- junction of the switch.

propagating in the [011] direction (i.e., polarized along $[0\bar{1}1]$) will experience an index decrease, while a TE wave propagating in the $[0\bar{1}1]$ direction (i.e., polarization along [011]) will experience an index increase. Since the electro-optic index changes are the same order of magnitude as the effective guide index difference that maintains the lateral mode confinement, switches fabricated for propagation along these two different orientations will have different performance characteristics, as illustrated in the next two figures.

Figure I-3 shows typical data for a switch oriented for propagation along a $[0\bar{1}1]$ direction. The switch length was approximately that of the computed coupling length (L = 8.2 mm). The
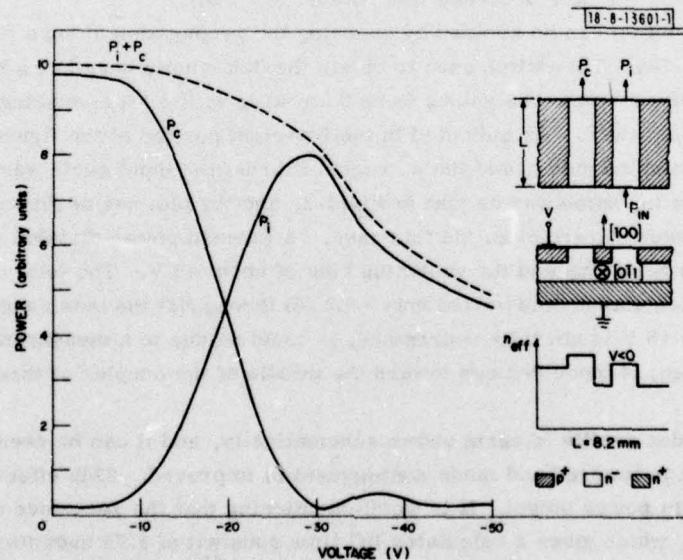
Fig. I-3. Power vs bias for each channel of a GaAs $p^+n^-n^+$ directional-coupler switch for propagation in a $[0\bar{1}1]$ direction. The diagrams to the right illustrate, from top to bottom, the optical arrangement, the biasing scheme, and a schematic effective-index profile.

3

guides were 6 μm wide with a 6-μm spacing, and the epitaxial layer was 4.8 μm thick. As shown in the top-right portion of the figure, the light was incident in the guide furthest away from the biased p^+ region. The power output vs bias from the coupled channel P_c and input channel P_i are plotted along with the total power, $P_c + P_i$. The plot has been normalized to the total output power at zero bias. As shown here, the light was 98 percent (17 dB) coupled at zero bias and 3-dB switching was achieved at ~20 V. Maximum switching occurred at ~30 V bias, with 97.5 percent (16 dB) of the total power emerging from the input channel. The total output power decreased about 0.8 dB between 0 and 30 V bias, and continued to fall off gradually at higher biases.

The bottom-right figure is a schematic representation of the effective-index profile in the switch for this orientation at an arbitrary negative bias. The two high-index regions represent the effective index in the central guiding regions, and as previously mentioned, account for the lateral confinement of the propagating light. For propagation in a [0$\overline{1}$1] direction, reverse-biasing the p^+n^- junction raises the index on the left, as shown. This effectively reduces the mode confinement in the left guide and leads to the decrease in total output power. This sketched effective-index profile is only diagrammatic. This is especially true in the left central guiding region where it is difficult to determine the shape and magnitude of the effective index because of the combined effects of index changes caused by the vertical component of the fringing field and changes induced by the electro-optic index variation directly under the biased p^+ region.

The effect of the reduced mode confinement was more evident when the bias was shifted to the outer p^+ region adjacent to the input guide. For this case, the 17-dB switching isolation was still obtained, but the total power fell off somewhat more rapidly, being 2 dB down at the optimum switching voltage. It is worth noting that this phenomenon allowed us to achieve 19-dB modulation of the power in the coupled guide by switching between zero and the optimum switching voltage. (By grounding the p^+ region nearest the input guide, the switching bias could be reduced so that the above power decrease was limited to ~1 dB.)

The power-loss effect can be avoided by choosing the propagation along a [011] direction, as illustrated in Fig. I-4. The switch used to obtain the data shown here had a length (approximately equal to L) of 7.2 mm. The guides were 8 μm wide with 4.5-μm spacing, and the epitaxial layer was 4.8 μm thick. As indicated in the top-right portion of the figure, the bias was applied nearest the coupled guide, and the p^+ region nearest the input guide was grounded. The data were obtained in the same way as that in Fig. I-3, and the plot has again been normalized to the total output power at zero bias. In this case, 98-percent power division (17-dB isolation) was achieved at both zero bias and the switching bias of about 43 V. The total output power was constant at both switch states, and varied only ~0.2 dB throughout the bias range. The small power dip near V = −15 V is not fully understood; it could be due to a measurement effect resulting from movement of mode centers toward the middle of the coupler at these intermediate biases.

The effective-index profile is again shown schematically, and it can be seen that for this orientation the index is lowered and mode confinement is improved. This effect, we believe, results in the constant power output. It is worth mentioning that the zero-bias capacitance of this switch is 35 pF, which gives a calculated RC time constant of 1.75 nsec for the device in a 50-Ω system. This corresponds to a power-bandwidth ratio[13] for maximum switching of 110 mW/MHz. This should not be an upper performance limit since a reduction of the capacitance by about an order of magnitude could be realized by shrinking the width of the p^+ regions.

4

18-8-13600-2
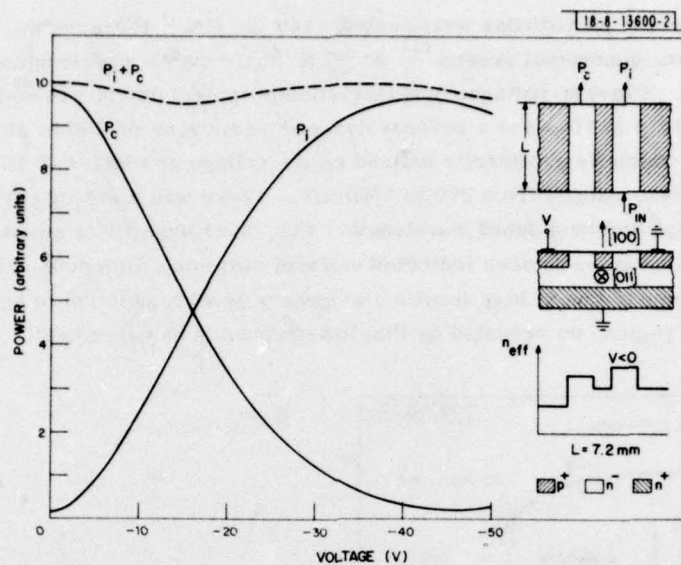
Fig. I-4. Power vs bias for each channel of a GaAs $p^+n^-n^+$ directional-coupler switch for propagation in a [011] direction. The diagrams to the right illustrate, from top to bottom, the optical arrangement, the biasing scheme, and a schematic effective-index profile.

In conclusion, GaAs $p^+n^-n^+$ directional-coupler switches have been fabricated in lengths of 7.2 to 8.2 mm. These lengths suggest the feasibility of integrating the switches with other components on a GaAs wafer of workable dimensions. Optimum switching biases achieved are $\leqslant 45$ V, with 17-dB isolation in both the switched and unswitched states. Finally, it has been found that the performance of the switches is orientation dependent, and that essentially constant output power is obtained for switches fabricated on {100}-oriented material and designed for propagation in a [011] direction.

F. J. Leonberger
J. P. Donnelly
C. O. Bozler

B. HIGH-FREQUENCY CHARACTERIZATION OF HgCdTe PHOTODIODES

Proper characterization of HgCdTe photodiodes for use as GHz-response CO_2 laser heterodyne receivers requires uniformity and sensitivity measurements in the operating frequency region. Quantum efficiency and uniformity data obtained from the conventional low-frequency (< 1 kHz) measurements are not necessarily indicative of performance in the GHz region. These conclusions have been drawn from numerous high-frequency measurements described below which were carried out on Hg-diffused, n- on p-type HgCdTe photodiodes.[14,15] Over 100 discrete devices were evaluated by two or more of the following six different measurements: pulse response, high-frequency raster scan profiles, RF noise output as a function of detector bias and frequency, direct heterodyne detection, and blackbody heterodyne radiometry.[15,16] Some unique techniques were employed in these measurements to minimize potential sources of error and improve reliability and reproducibility. The 3-dB rolloff frequency of the photodiodes tested ranged from about 500 MHz to over 2 GHz. At these frequencies the heterodyne sensitivity (MDP) of these devices typically ranged from about 3×10^{-20} to 1×10^{-19} W/Hz.

5

Three different-size photodiodes were tested: 110-μm-dia., 160-μm-dia., and single ele-
ments of 300-μm-dia. quadrantal arrays.[17] At 77 K, their cutoff wavelengths ranged from
about 11 to 14.5 μm. Current-voltage characteristics of typical devices revealed a limiting
forward resistance of 5 to 10 Ω and a reverse dynamic resistance of 200 to 20,000 Ω. The
breakdown voltage, which we arbitrarily defined as the voltage at which 1/2 mA of excess re-
verse current is drawn, ranged from 200 to 1500 mV. There was a strong correlation between
low breakdown voltage and long cutoff wavelength. CO_2 laser sensitivity scans across the
active area of these uncoated devices indicated uniform quantum efficiencies ranging from about
0.4 to 0.7. The devices tested at high frequencies generally were uniform to better than ±10 per-
cent over the active region, as revealed by this low-frequency measurement.
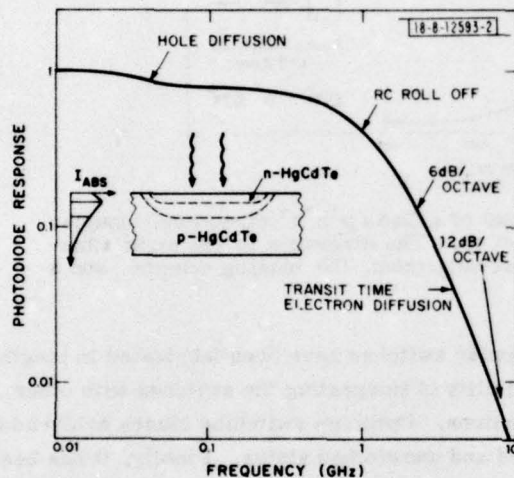
Fig. I-5. Frequency response of a typical high-speed HgCdTe photodiode.

The expected frequency response of a typical reverse-biased HgCdTe photodiode is shown
in Fig. I-5. There is very little frequency dependence up to about 50 MHz, at which point slow
diffusion of holes generated in the n-type region gives rise to a drop in response. The magni-
tude of this drop, of course, depends upon the amount of radiation absorbed in the n-type re-
gion, i.e., the thickness of the n-type layer and the absorption coefficient. The next effect on
the frequency response is the RC rolloff, which is found to vary as the square-root of the bias
voltage, in agreement with capacitance measurements. Transit time across the depletion re-
gion (~1 to 2 μm wide at maximum bias) and electron diffusion to the junction from the p-type
region manifest themselves in the 2- to 10-GHz region, beyond which a 12-dB/octave rolloff is
seen.[14] The latter three effects have not been clearly resolved experimentally for frequencies
much greater than 1 GHz.

For sensitive heterodyne detection, the photodiode must be illuminated with local oscillator
power at levels of the order of 1 mW, which alters the response shown in Fig. I-5. These high
power densities ($\gtrsim 10$ W/cm^2) generate high non-equilibrium free-electron densities[18] which
(a) fill the conduction band, thereby reducing the absorption coefficient, and (b) increase the
probability of Auger recombination.[19] Both effects reduce the quantum efficiency of the de-
tector. This non-equilibrium electron concentration can be much larger than the equilibrium
concentration in the n-type region (~5×10^{14} cm^{-3}), which tends to shrink the depletion width

and raise the capacitance of the device. In other words, the RC rolloff frequency decreases with increasing local oscillator power. Exact quantitative details of these effects and other possible high power saturation phenomena are not understood. They are expected to be dependent upon the precise energy gap of the HgCdTe, equilibirum electron and hole concentrations, and junction depth, all of which vary from device to device. Thus, the only way to be certain of the high-frequency heterodyne sensitivity of a particular device is to carry out a direct measurement.

1. Pulse Response Measurements

Pulse response data were used to obtain the frequency response of the photodiode up to about 1 GHz. A CO_2 laser beam, a $0.3 \times 0.3 \times 10$-mm^3 of CdTe electro-optic polarization modulator driven by a mercury switch pulser, and a sampling oscilloscope were used for these measurements. Examples of type of data obtained on two photodiodes are shown by oscilloscope display photographs in Fig. I-6. The two photodiodes, which had similar low-frequency characteristics, were biased at 500 mV for the measurements. The device on the left shows rise and

29A-1   27-4   -8-12574-1

($V_B = 0.5$V)   ($V_B = 0.5$V)

|← →| |← 2nsec |← →| |← 2nsec
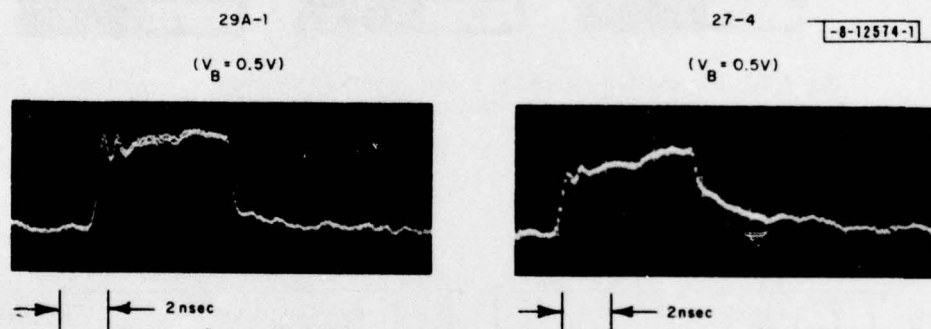
Fig. I-6. Oscilloscope displays showing the pulse response of two reverse-biased HgCdTe photodiodes.

fall times of less than 0.3 nsec, the response of the electronics. The device on the right shows similar fast initial rise and fall times, but in addition has a slow (~3 nsec) component which represents about 1/2 of its total response. This slow component appears to be due to hole diffusion mentioned above. The relative magnitude of this 3-nsec response component decreases with increasing bias, which is to be expected since junction depletion consumes part of the n-type surface layer. In some devices, the relative magnitude of this hole diffusion component was found to vary from 10 to 80 percent over the active region. Presumably this was a consequence of an uneven junction depth and/or a nonuniform depletion layer width due to carrier concentration inhomogeneities in the n-type layer. Low-frequency sensitivity scans did not reveal any of these irregularities.

2. Uniformity at High Frequencies

Measurements of response uniformity in the high-frequency regime were made by driving the CdTe electro-optic modulator with a 1.2-GHz RF source, which put a 1.2-GHz amplitude modulation on the CO_2 beam. This modulated beam was raster scanned across the detectors
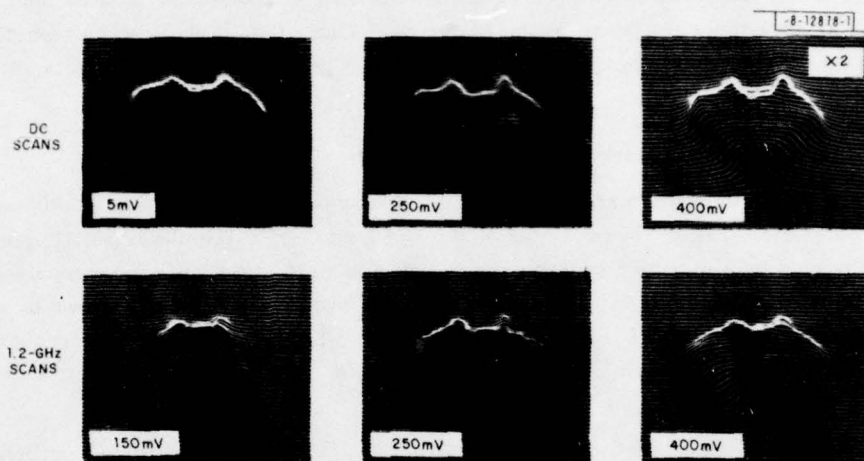
Fig. I-7. DC and 1.2-GHz CO_2 laser sensitivity scan profiles of one element of a HgCdTe quadrantal array taken for different values of detector bias.
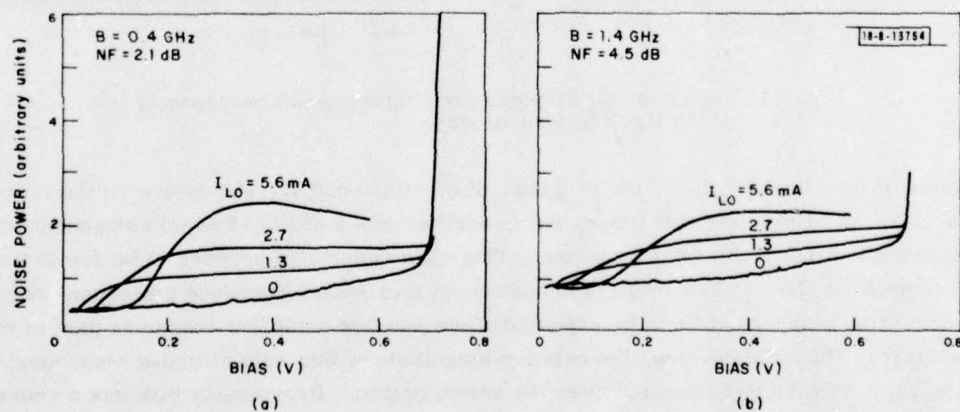
Fig. I-8. Amplifier output noise power as a function of photodiode bias for different levels of CO_2-local-oscillator-induced photocurrent: (a) 0.1- to 0.5-GHz amplifier bandwidth, 2.1-dB average noise figure; (b) 0.1- to 1.5-GHz amplifier bandwidth; 4.5-dB average noise figure.

using conventional galvanometer scanners synchronized with an oscilloscope. However, instead of feeding the detector signal directly into the y-axis of the scope, it was first fed into a low-noise, high-gain RF amplifier and a spectrum analyzer tuned to 1.2 GHz. The rectified output from the spectrum analyzer was then fed into the scope. Figure I-7 is an example of the raster scan profiles obtained with the system. The upper three photographs are response profiles of one of the photodiodes from a 300-μm-dia. quadrantal array[17] taken at three different biases by the conventional DC method. The response is quite uniform at all three bias levels. A decrease in detector impedance with increasing bias is responsible for the factor-of-two drop in signal from 5 to 400 mV. At 1.2 GHz, no response is detected unless a bias of about 150 mV is applied, and then the response is not uniform as shown by the lower left-hand photograph in Fig. I-7. The device is sensitive only near the bonding pad. Now as the bias is increased to where the RC rolloff is about 1.2 GHz, the response becomes very uniform over the entire active area. Unfortunately, this was not the case for all devices. Some have shown a very peaked response around the perimeter, indicating an excessively deep junction. Others have shown a graded response similar to the 150-mV scan, possibly due to an excessive sheet resistance in the n-layer. About half the devices tested were uniform at 1.2 GHz. Generally, most of the devices from a given fabrication run had similar properties.

3. Noise Measurements

Since good heterodyne sensitivity requires local oscillator shot-noise-limited operation, potential noise sources must be examined. A relatively simple test for excess noise is a measurement of noise as a function of detector bias. This is easily done by connecting a high-gain, low-noise preamplifier to the photodiode and measuring the amplifier output noise with a crystal detector. Figures I-8(a) and -8(b) are results of such measurements which show the total noise power over the amplifier bandwidth as a function of detector bias for a typical HgCdTe photodiode. In the case of Fig. I-8(a), the preamplifier had a 0.1- to 0.5-GHz bandwidth and an average noise figure of about 2.1 dB, whereas in Fig. I-8(b) a 0.1- to 1.5-GHz bandwidth preamplifier was used with a 4.5-dB average noise figure. The four curves correspond to different levels of CO_2 local oscillator power (from zero to 1.3 mW) as indicated by the photocurrents. With the local oscillator off, the noise level is independent of bias from zero to 0.3 V, then increases slowly with bias to about 0.7 V where a large increase occurs. The latter effect is clearly indicative of avalanche breakdown. Current-voltage characteristic of this photodiode indicated a "soft" breakdown typical of most devices, with a breakdown voltage (as defined above) of 350 mV. The slow increase in noise beginning at 0.3 V apparently associated with this soft breakdown could be a result of small localized avalanche regions in the device. In general, the current-voltage characteristic is not a reliable indicator of the bias-dependent RF noise component. Devices with nearly identical I-V characteristic have shown greatly different RF noise-vs-bias curves. The device of Fig. I-8 is typical, i.e., other devices have shown stronger or weaker bias dependence.

With the CO_2 local oscillator focused to a 60- to 80-μm spot diameter on the device, the noise level increased significantly, particularly when the 2.1-dB noise figure preamplifier was used. The drop in shot noise at low bias is a consequence of the detector bandwidth being less than the amplifier bandwidth. Also, IR drop across the series resistance in the detector decreases the effective junction bias. The decrease in shot noise with increased bias in the 5.6-mA curve in Fig. I-8(a) is a consequence of a decrease in RF impedance of the photodiode.

9

The shot noise seen with the 2.1-dB amplifier agrees with that calculated, whereas with the 4.5-dB amplifier the shot noise observed is about 40 percent less than calculated, indicating that the detector bandwidth is less than the 1.5-GHz amplifier bandwidth. In some devices, the shot noise varied considerably when the local oscillator was moved over the active region of the device. The position on the detector at which maximum DC photocurrent was obtained was not the position of maximum shot noise and heterodyne sensitivity. The reason for this behavior in source devices is not fully understood.

An example of the frequency dependence of the shot noise obtained with a spectrum analyzer is shown in Fig. I-9. The RC rolloff of the device is obtained from this measurement. The measurement, however, is not sensitive to the effects of hole and electron diffusion on the frequency response. Heterodyne sensitivity cannot be deduced from these data as the high-frequency, differential quantum efficiency at the particular local oscillator power level is not directly indicated. Nonetheless, it is a convenient way of measuring the RC rolloff, which for the device of Fig. I-9 is over 2 GHz.
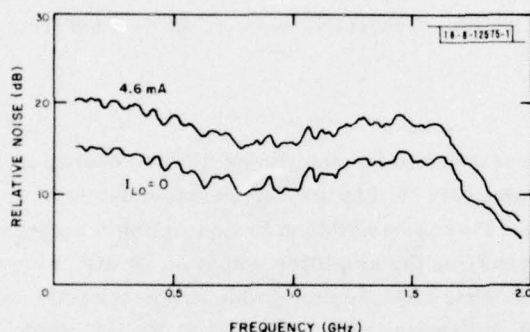
Fig. I-9. Relative amplifier output noise as a function of frequency for a reverse-biased HgCdTe photodiode with 0 and 4.6 mA of photocurrent.

4. Heterodyne Beat Measurements

Direct heterodyne sensitivity measurements were carried out using a germanium acousto-optic modulator to generate a second coherent beam, offset in frequency from the CO_2 output. This technique has many advantages over other direct heterodyne measurements reported.[14,18,20] The sideband generated by the acousto-optic modulator is diffracted away from the incident beam, producing a highly isolated sideband. The diffracted optical power is linear with RF input power (at low power levels), enabling precise attenuation of the optical beam with calibrated RF attenuators. The modulator has a diffraction efficiency of about 10 percent per watt of RF power; thus, it can produce sufficient sideband power to make optical alignment relatively simple. An optical sideband offset by 80 MHz was produced by passing the optical beam through the 40-MHz modulator twice. This moves the optical beat frequency away from the RF generator frequency and eliminates potential crosstalk. In the measurements, the unmodulated CO_2 beam and the sideband were mixed on a beam splitter and focused to a 60- to 80-μm-dia. spot on the detector. With the local oscillator beam blocked, the sideband power was measured by the photocurrent produced in the detector. A precision 40-dB attenuator was then inserted between the modulator and the RF driver, which dropped the optical sideband power by 80 dB to a level of the order of 10^{-13} W. Heterodyne sensitivity was then determined simply from this directly measured power, the signal-to-noise ratio of the beat signal, and the IF bandwidth. The detector area and the transmission of the optics do not enter into the sensitivity calculation. Photodiode heterodyne

minimum detectable powers deduced from these measurements typically ranged from $3.0 \pm 0.6 \times 10^{-20}$ to about 1×10^{-19} W/Hz. We are in the process of RF matching to the seventh harmonic of the acoustic transducer in order to generate a 560-MHz optical sideband and repeat the above measurements closer to the rolloff frequencies of the detectors.

5. Blackbody Heterodyne Radiometry

Blackbody heterodyne radiometry has been used previously to measure detector sensitivity.[15,21] However, by simply inserting an RF sweep oscillator and mixer in the detection circuit, heterodyne MDP can be directly measured as a function of frequency. Except for response uniformity, this gives all the critical parameters needed for most heterodyne receivers. The measurement system is the same as that described previously[16] for heterodyne spectroscopy measurements. Instead of plotting heterodyne signal vs frequency on the x-y recorder, signal to noise was plotted vs frequency by using the noise output option of an Ithaco Dynatrac lock-in amplifier and a ratiometer. Figure I-10 is an example of these data taken in two 100-sec frequency sweeps of 0.4 to 2 GHz and 2 to 4 GHz. The fall-off near the end of the 0.4- to 2-GHz trace is a result of the 0.3-GHz resolution used. The device shows a cutoff frequency of about 1.2 GHz. An effective quantum efficiency (η) of device (and preamplifier) can be calculated from the measured signal to noise using the theoretical expression for the signal-to-noise ratio of blackbody heterodyne detection,[22]

$$S/N = 2\eta \ (B\tau)^{1/2} \ T_t/[\exp (h\nu/kT) - 1] \quad ,$$

where B is the RF detection bandwidth, τ is the post-detection integration time, T is the temperature of the blackbody source, and T_t is the transmission of the optics between the source and detector. The effective quantum efficiencies obtained for most of our devices were in the range 0.5 ± 0.1 to 0.15 at 750 MHz. The best values are in agreement with the results obtained with the acousto-optic modulator. Heterodyne radiometry has the advantage of a very wide bandwidth capability, being limited only by the RF components used to process the heterodyne signal.

Fig. I-10. Blackbody heterodyne signal-to-noise ratio as a function of frequency.
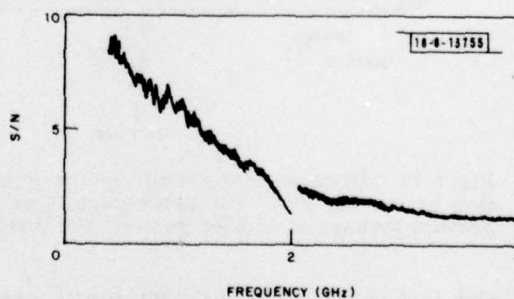
Six measurements have been described for high-frequency characterization of GHz-response HgCdTe photodiodes. Extensive device evaluation has shown that low-frequency uniformity and quantum efficiency data are not reliable measures of high-frequency performance.

D. L. Spears

C. TEMPERATURE-GRADIENT LPE GROWTH OF $Pb_{1-x}Sn_xTe$

A temperature-gradient growth apparatus for liquid-phase epitaxy (LPE) has been constructed. Growth of $Pb_{1-x}Sn_xTe$ alloys with this apparatus demonstrates that the induced temperature gradient (1) does not improve the growth quality of heteroepitaxial growth in the $Pb_{1-x}Sn_xTe$ system, and (2) does not have a measurable effect on the Sn/Pb ratio of the epitaxial growth.

Very favorable results have been reported for LPE growth under conditions of a strong temperature gradient normal to the substrate-solution interface.[23-27] These are most readily interpreted as being due to an increased nucleation density that occurs from an enhanced supersaturation of the solution, at the growth interface, caused by the temperature gradient. The present study was undertaken because relatively little supersaturation of the Pb-Sn rich growth solutions is possible, and efforts to obtain greater supersaturation generally have resulted in improved growth.[28] This, in turn, has resulted in improved performance of diode lasers fabricated from the LPE growth. A second reason for this study was to explore the possibility that the Sn/Pb ratio in the grown solid is a function of the temperature gradient, a possibility suggested by a discrepancy, to be explained below, between our liquid-solid tie-line data and those reported by Harris et al.,[29] taken with the apparatus reported in Refs. 24 and 26.
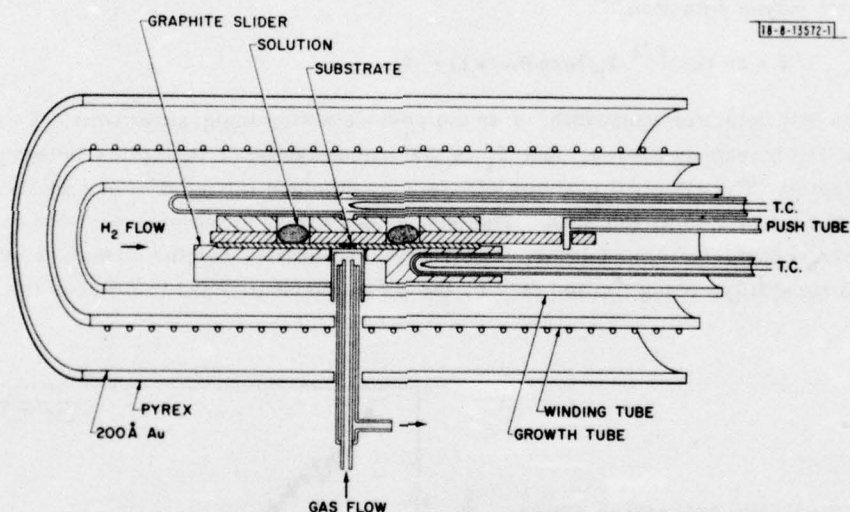
Fig. I-11. Drawing of the temperature-gradient LPE apparatus featuring a radial flow of cooling gas. Fit between gas flow tube and growth tube is tight enough to prevent leakage of cooling gas into the furnace.

Figure I-11 is a drawing of the temperature-gradient LPE apparatus. By using a transparent furnace, where the insulation is a thin, reflecting layer of gold on the inside diameter of a Pyrex tube,[30] it is possible to fabricate and assemble an apparatus in which the cooling gas enters radially and, thus, does not introduce the large horizontal temperature gradient that would be present if the cooling gas were brought down the bore of the furnace. To insure low thermal resistance between the cooling tube and the substrate, a thin piece of graphite (1 mm) is used for the substrate holder, and this is pressed into good contact with the cooling tube by

a twist of the eccentric thermocouple tube. Precision O. D. and I. D. tubing is used in the cooling assembly to prevent the escape of gas into the furnace. The bore of the flow tube is 3 mm. With modest pressures of 5 to 10 psi, it is possible to get sizeable gas flows of $\sim 5 l$/min. which, in turn, produce temperature gradients estimated to be between 5° and 10°C/cm.

To test the effect of the induced temperature gradient on growth morphology, $Pb_{1-x}Sn_xTe$, with $x \simeq 0.12$, was grown on PbTe substrates misorientated by $\frac{1}{4}°$ or more from the (100) plane. Initial growth studies in an apparatus without the induced temperature gradient showed that these conditions consistently produce terraces or hills, as shown in Fig. I-12(a). Use of an increasing flow of cooling gas to apply a temperature gradient and to maintain a constant $\frac{1}{3}°$/min. cooling[29] gave the results shown in Fig. I-12(b) which are comparable to those of Fig. I-12(a). Application of larger temperature gradients by higher gas flows gave rougher growth. With very high flows of cooling gas, Sn droplets developed as a growth imperfection.[31] The conclusion drawn from these results is that the induced temperature gradient does not improve growth quality for the case of $Pb_{1-x}Sn_xTe$ grown on PbTe. One may speculate that either the induced temperature gradient does not increase the supersaturation at the growth interface, or that a greater degree of supersaturation and higher nucleation density will not cure the particular growth defect we have chosen to test. Some support for the latter point of view comes from the observation that smooth growth is obtained either by matching lattice constants of the epilayer and the substrate, or by having a growth surface accurately oriented to the (100) plane, an example of which is shown in Fig. I-12(c). These are factors that, presumably, do not increase the nucleation density. This would leave open the possibility that the temperature gradient apparatus can improve growth in cases where a low nucleation density limits the growth quality. Growth of PbS and

(a)

(b)

(c)
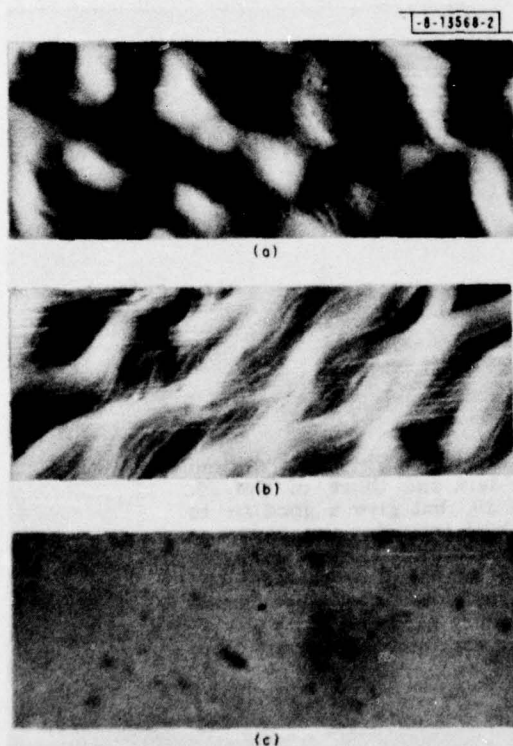
Fig. I-12. Micrographs of three LPE growths of $Pb_{0.88}Sn_{0.12}Te$ approximately 15 μm thick on PbTe substrates. Growth was initiated at $T \simeq 640°C$. (a) Zero induced gradient, controller programmed to cool at 0.3°C/min. (b) Furnace held at constant temperature, flow of cooling gas induces gradient and causes substrate to cool at 0.3°C/min. Surface roughness is comparable to that shown in (a). (c) Very smooth growth produced by either (a) or (b) conditions when growth plane of substrate is accurately aligned to (1,0,0), here obtained by growth on a facet from a vapor-grown crystal.

$PbS_{1-x}Se_x$ on PbS may be such a case because of the relatively poor quality of etched PbS surfaces. Experiments are planned to test the growth of these alloys in the temperature-gradient apparatus.

Figure I-13 shows liquid-solid tie-line data relating the Sn/Pb ratio in the liquid to that in the grown solid. The open triangles are data from our earlier work in an apparatus without an induced temperature gradient. The solid lines, in poor agreement with the triangles, result from a modified simple solution calculation by workers at the Rockwell Science Center.[29] This calculation uses empirically determined interaction parameters, and fits the Rockwell experimental data (not shown) well enough in the region shown to be taken, for purposes here, as a curve through their experimental points. The primary difference between our growth technique and that of the Rockwell workers was their use of the induced temperature gradient technique. The idea that this could influence the Sn/Pb ratio in the solid gains some plausibility from the fact that LPE growth of GaAlAs by Peltier cooling apparently produces different behavior of the Al/Ga ratio than conventional LPE growth,[32] and the Peltier cooling also produces a temperature gradient at the substrate-solution interface.

All growths made in the present study were from a solution with a Sn/Pb ratio of 0.22/0.78. The grown layers were analyzed by electron microprobe, and the results are shown as solid triangles in Fig. I-13. The three points with $\bar{x} \geqslant 0.12$ come from the growths shown in Fig. I-12 with $\frac{1}{3}°C$/min. cooling; the highest and lowest of these were grown with the induced temperature gradient. The three points with $\bar{x} \leqslant 0.12$ were grown, in order of decreasing $\bar{x}$, at $2°C$/min. caused by the cooling gas, at $3°C$/min. caused by a higher flow of cooling gas, and at $3°C$/min. programmed on the controller and no induced gradient. The maximum uncertainty of the microprobe determination of $\bar{x}$ is ±0.02; within that, we can apparently detect some dependence of $\bar{x}$
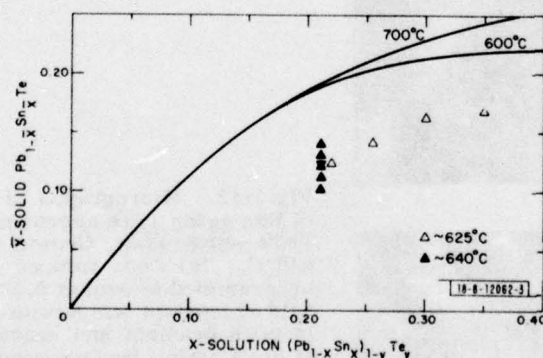
Fig. I-13. Liquid-solid tie-line data for the Pb-Sn-Te system showing discrepancy between our data and those of Ref. 29. Lines are from calculation of Ref. 29, but give a good fit to the experimental data of Ref. 29. Open triangles are from our previous work in a conventional apparatus. Closed triangles are from the present work with the temperature-gradient apparatus. The scatter of the solid triangles cannot be explained by cooling rate or amount of temperature gradient; it is attributed to the uncertainty in the electron microprobe determination.

on rate of cooling but not on the induced temperature gradient. In any case, the range of values we observe definitely falls outside the results of Ref. 29. This has motivated the Rockwell workers to make a redetermination of the tie-line data with the growth apparatus that is presently being used and which does not use an induced temperature gradient. Their new data are in agreement with ours in Fig. I-13 to within experimental uncertainties, but the reason for the discrepancy with the earlier work is still unknown.[33]

In conclusion, a temperature-gradient LPE apparatus has been constructed which permits a large temperature gradient normal to the substrate-solution interface with minimum unwanted gradients along the bore of the furnace. Tests with the $Pb_{1-x}Sn_xTe$ growth show that the induced gradient does not improve growth morphology over that obtained by state-of-the-art conventional techniques. Experiments on the growth of $PbS_{1-x}Se_x$ alloys with the induced temperature gradient technique are planned. Finally, the induced temperature gradient does not measurably affect the Sn/Pb ratio of the grown layer, and thus does not explain the discrepancy between the currently accepted tie-line data and those obtained previously using the temperature-gradient growth technique. A more detailed account of this work has been submitted for publication.

<div align="right">S. H. Groves</div>

REFERENCES

1. F. J. Leonberger, J. P. Donnelly, and C. O. Bozler, Appl. Phys. Lett. **28**, 616 (1976), DDC AD-A027103.

2. Solid State Research Report, Lincoln Laboratory, M. I. T. (1976:2), p.4.

3. S. Kurazono, K. Iwasaki, and M. Kumagai, Electron. Commun. Jap. **55-C**, 103 (1972).

4. H. F. Taylor, J. Appl. Phys. **44**, 3257 (1973).

5. S. Somekh, E. Garmire, A. Yariv, H. L. Garvin and R. G. Hunsperger, Appl. Opt. **13**, 327 (1974).

6. K. Tada and K. Hirose, Appl. Phys. Lett. **25**, 561 (1974).

7. J. C. Campbell, F. A. Blum, D. W. Shaw and K. L. Lawley, Appl. Phys. Lett. **27**, 202 (1975).

8. J. P. Donnelly, F. J. Leonberger and C. O. Bozler, Appl. Phys. Lett. **28**, 706 (1976).

9. J. P. Donnelly, W. T. Lindley, and C. E. Hurwitz, Appl. Phys. Lett. **27**, 41 (1975), DDC AD-A016690/0.

10. Y. Tarui, Y. Kamiya and Y. Harada, J. Electrochem. Soc. **118**, 118 (1971).

11. H. C. Gatos and M. C. Lavine, J. Electrochem. Soc. **107**, 427 (1960).

12. See, for example, D. F. Nelson and J. McKenna, J. Appl. Phys. **38**, 4057 (1967).

13. I. P. Kaminow and E. H. Turner, Proc. IEEE **54**, 1374 (1966).

14. Solid State Research Report, Lincoln Laboratory, M. I. T. (1973:2), p. 2. DDC AD-766233/1.

15. Ibid (1974:4), p. 5, DDC AD-A004763/9.

16. Ibid (1975:3), p. 3, DDC AD-A019472/0.

17. <u>Ibid</u> (1975:1), p. 1, DDC AD-A009848/3; also, D. L. Spears, Infrared Physics (to be published).

18. C. Verié and M. Sirieix, IEEE J. Quant. Electron. <u>QE-8</u>, 180 (1972).

19. F. Bartoli, R. Allen, L. Esterowitz, and M. Kruer, J. Appl. Phys. <u>45</u>, 2150 (1974).

20. B. J. Peyton, A. J. DiNardo, G. M. Kanischak, F. R. Arams, R. A. Lang, and E. W. Sard, IEEE J. Quant. Electron. <u>QE-8</u>, 252 (1972).

21. J. Gay, A. Journet, B. Christophe and M. Robert, Appl. Phys. Lett. <u>16</u>, 448 (1973).

22. J. H. McElroy, Appl. Optics <u>11</u>, 1619 (1972).

23. J. A. Donahue and H. T. Minden, J. Cryst. Growth <u>7</u>, 221 (1970).

24. J. T. Longo, J. S. Harris, E. R. Gertner and J. C. Chu, J. Cryst. Growth <u>15</u>, 107 (1972).

25. B. L. Mattes and R. K. Route, J. Cryst. Growth <u>16</u>, 219 (1972).

26. J. T. Longo, E. R. Gertner and J. S. Harris, J. Nonmetals <u>1</u>, 321 (1973).

27. I. Kasai and D. W. Bassett, J. Cryst. Growth <u>27</u>, 215 (1974).

28. Solid State Research Report, Lincoln Laboratory, M. I. T. (1974:2), p. 17, DDC AD-783634/9.

29. J. S. Harris, J. T. Longo, E. R. Gertner and J. E. Clarke, J. Cryst. Growth <u>28</u>, 334 (1975).

30. Solid State Research Report, Lincoln Laboratory, M. I. T. (1969:1), p. 21, DDC AD-687100.

31. <u>Ibid</u> (1974:4), p. 13, DDC AD-A004763/9.

32. J. J. Daniele, Appl. Phys. Lett. <u>27</u>, 373 (1975).

33. J. T. Longo, C. C. Wang, and J. S. Harris, unpublished results.

A. FLUORESCENCE AND LASING PROPERTIES OF $NdNa_5(WO_4)_4$, $K_3Nd(PO_4)_2$, AND $Na_3Nd(PO_4)_2$

We have studied fluorescence and lasing in three new materials containing Nd as a stoichiometric constituent. The crystal growth and structure (tetragonal, $I4_1/a$) of the first of these, $NdNa_5(WO_4)_4$ (Nd sodium tungstate, abbreviated NST), have been reported by Hong and Dwight.[1] Using collinear excitation by a CW dye laser tuned to the 0.58-μm Nd^{3+} absorption band, we have achieved lasing in NST crystals approximately 0.5×0.5 mm in area and 0.1 to 0.2 mm long in the lasing direction. Threshold absorbed powers as low as 330 μW and optical power conversion efficiencies up to 22 percent have been achieved using a 1.1-percent transmitting output mirror. With crystal losses of ~1 percent, determined by analysis of the laser relaxation oscillations, a maximum external power efficiency of 28 percent is calculated for 0.586-μm excitation and 1.1-percent output transmission.

From the measured threshold power and the values of the laser saturation parameter obtained from the relaxation oscillations, the peak laser cross section at 1.063 μm is estimated to be 5 to 10×10^{-19} cm^2, considerably larger than the maximum cross section of 2×10^{-19} cm^2 in NdP_5O_{14} (Ref. 2). Calculation of the cross sections from fluorescence (Fig. II-1) and absorption data gives a value somewhat smaller than the above estimate, but is subject to large sources of error. Although the Nd concentration in NST (2.6×10^{21} cm^{-3}) is considerably lower than that in NdP_5O_{14} (3.9×10^{21} cm^{-3}), the absorption coefficient of pump radiation in NST is ~200 cm^{-1}, resulting in well over 80 percent pump absorption in crystals only 0.1 mm thick. The large emission cross section, low threshold, and strong pump absorption in NST compare favorably with these parameters in other high-Nd-concentration laser compounds, making NST an attractive candidate for further laser device development.
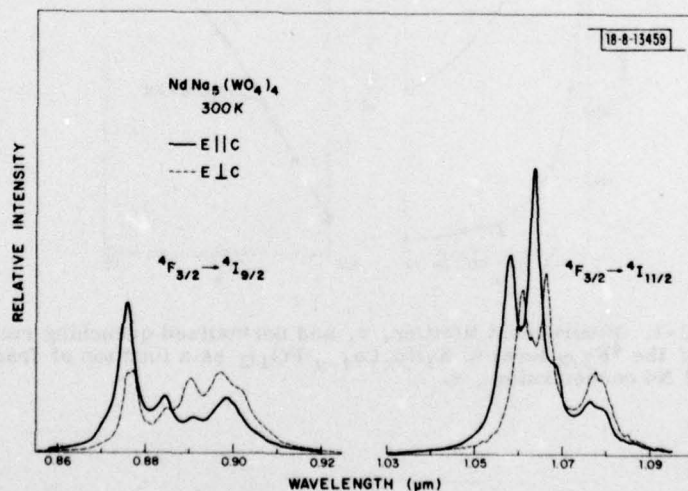
Fig. II-1.   Polarized room-temperature fluorescence spectra of $NdNa_5(WO_4)_4$.
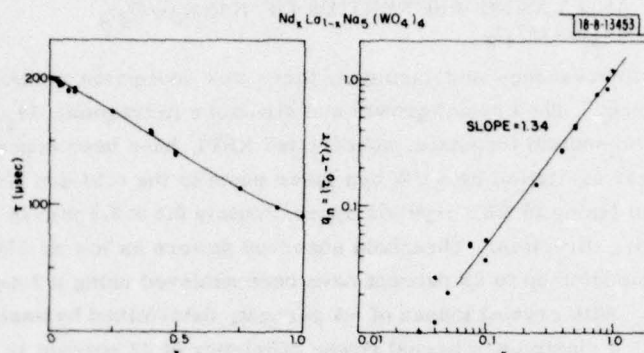
Fig. II-2. Fluorescent lifetime, τ, and normalized quenching rate, q_n, of the $^4F_{3/2}$ level in $Nd_xLa_{1-x}Na_5(WO_4)_4$ as a function of fractional Nd concentration, x.
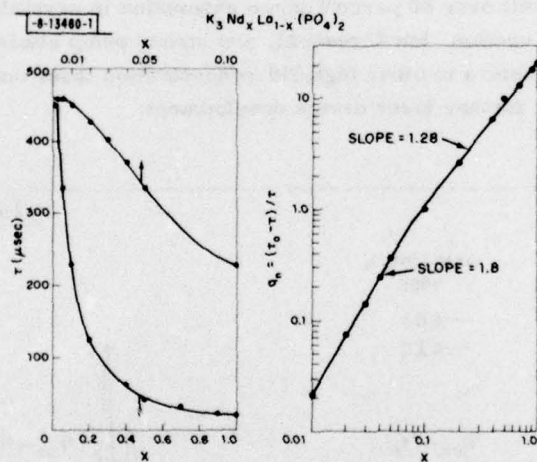
Fig. II-3. Fluorescent lifetime, τ, and normalized quenching rate, q_n, of the $^4F_{3/2}$ level in $K_3Nd_xLa_{1-x}(PO_4)_2$ as a function of fractional Nd concentration, x.

We have also studied the spontaneous emission as a function of Nd concentration in single crystals of $Nd_xLa_{1-x}Na_5(WO_4)_4$ for which the data are shown in Fig. II-2. The $^4F_{3/2}$ fluorescent lifetime is quenched from ~220 μsec at low Nd concentration to 90 μsec at x = 1. For values of x above 0.1 to 0.2, the fluorescence quenching rate increases linearly with x, in a manner similar to that observed for NdP_5O_{14} (Refs. 1,3), $LiNdP_4O_{12}$ (Refs. 4,5), and $NdAl_3(BO_3)_4$ (Ref. 6).

The other new materials are two orthophosphates $K_3Nd(PO_4)_2$ and $Na_3Nd(PO_4)_2$ (abbreviated KNOP and SNOP, respectively), which are grown by a flux method and have similar structures. The space group for KNOP is monoclinic, $P2_1/m$, with lattice parameters a = 9.532 Å, b = 5.631 Å, c = 7.444 Å, z = 2, and β = 90.95°, giving a Nd ion concentration of 5.0×10^{21} cm^{-3}. This material, like NdP_5O_{14}, $LiNdP_4O_{12}$, and $KNdP_4O_{12}$, has Nd ions linked by phosphate groups. However, unlike these materials in which corner-shared phosphate tetrahedra connect only two Nd ions, KNOP has single PO_4 tetrahedra connecting three Nd ions, with some of the phosphate groups sharing an edge with a neighboring Nd. Such coordination gives a layer-like structure with short Nd-Nd nearest-neighbor separations. As shown in Fig. II-3, the $^4F_{3/2}$ fluorescence lifetime decreases from 458 μsec in $K_3Nd_{0.005}La_{0.995}(PO)_4$ to 21 μsec in KNOP, and a logarithmic plot of quenching rate vs Nd concentration shows a high-concentration slope of ~1.3 rather than ~1.0, the value found for most other slightly quenched high-Nd-concentration laser compounds.[6] This change in concentration dependence may result from the different Nd coordination in KNOP.

The largest crystal of KNOP that has lased is 0.7 mm long in the lasing direction. The threshold (for a 1.1-percent transmitting output mirror) was 7.5 mW, and the power conversion efficiency was 17 percent. The maximum cross section at 1.055 μm is estimated to be 6 to 8×10^{-20} cm^2, in good agreement with results from fluorescence data (Fig. II-4) and absorption data. The pump absorption coefficient, 50 cm^{-1}, was much smaller than that of NST.

The crystal lattice of SNOP (space group possibly Pbcm) is a slightly distorted superstructure of KNOP, with a- and c-axes double, and b-axis triple, those of KNOP. Its lifetime behaves similarly to that of KNOP, decreasing from 359 μsec in $Na_3Nd_{0.005}La_{0.995}(PO_4)_2$ to
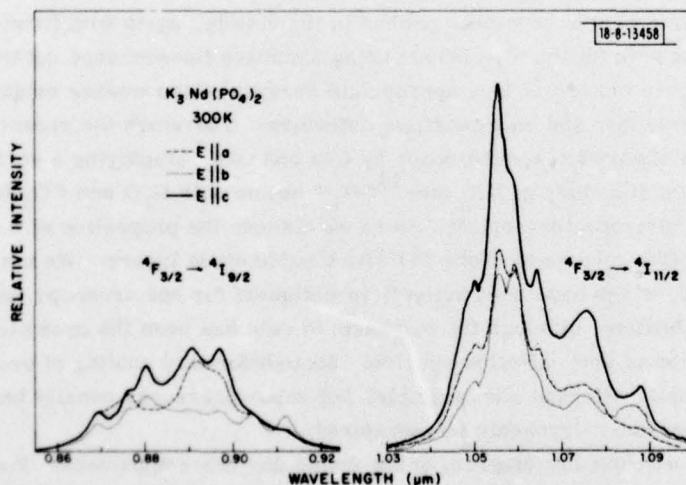
Fig. II-4. Polarized room-temperature fluorescence spectra of $K_3Nd(PO_4)_2$.

23 μsec in pure SNOP. Although lasing has been observed in SNOP, poor crystal quality has so far precluded a quantitative comparison with KNOP.

<div align="right">
S. R. Chinn
H. Y-P. Hong
</div>

B. SUBDOPPLER MOLECULAR BEAM INFRARED SPECTROSCOPY WITH TUNABLE DIODE LASERS

Doppler-broadening of spectral transitions in an ordinary gas obscures many fine structure details and masks some important molecular interactions. It is necessary therefore to reduce the Doppler-broadening to observe these phenomena. In this regard two general spectroscopic techniques capable of sub-Doppler resolution have been developed — first, atomic or molecular beam spectroscopy and second, nonlinear saturation spectroscopy. Nonlinear saturation spectroscopy includes Lamb-dip, level-crossing, two-photon, and modulated-population spectroscopy involving two counterpropagating laser beams of which at least one needs to be intense enough to saturate the population of the levels for the transition studied. Examples of these types of spectroscopy are too numerous to list here, but they have primarily been accomplished with fixed-frequency gas lasers in coincidence with a few molecular and atomic transitions. Such reliance on spectral coincidences for nonlinear spectroscopy has been obviated recently in the visible with the advent of tunable dye lasers. However, in the infrared, the broadly tunable lasers, such as the semiconductor and spin-flip Raman lasers, parametric oscillators, and other nonlinear optical devices, do not generally satisfy the combined requirements of narrow linewidth, high power, and feedback insensitivity to the counterpropagating light for saturation spectroscopy. To the present, we are aware of only one successful demonstration of nonlinear spectroscopy using tunable infrared lasers — a Lamb-dip measurement of water vapor with a spin-flip laser by Patel.[7] On the other hand, molecular beam spectroscopy, where the Doppler-broadening is reduced by simply propagating the light transverse to the molecular flow, would seem to be a more widely applicable technique for the non-ideal tunable infrared lasers available. We discuss here the use of tunable diode lasers to study sub-Doppler Λ-doubling in a nitric oxide beam.

Molecular and atomic beams have been probed in the visible, again with fixed-frequency laser coincidences, and with tunable dye lasers using sensitive fluorescence detection. In the infrared, the fluorescence method is less appropriate because of the weaker excitation sources, lower fluorescence efficiency, and less sensitive detectors. Therefore the recent demonstration of molecular beam absorption spectroscopy by Chu and Oka,[8] employing a series of effusive multitube collimators for the study of NH_3 and $^{13}CH_3F$ beams with N_2O and CO_2 lasers, is of great interest to molecular spectroscopists. Here we discuss the properties of a simplified version of the Chu and Oka scheme to probe NO with tunable diode lasers. We note that supersonic molecular beams, which have been actively investigated for spectroscopy recently, also have sub-Doppler capabilities, although the emphasis to date has been the dynamic cooling of the gas for simplification of very complex spectra. Straightforward cooling of ordinary gas cells to reduce the Doppler effect is also possible, but vapor pressures usually become prohibitively low at the necessary cryogenic temperatures.

Figure II-5 shows a schematic diagram of the molecular beam apparatus. Four multitube collimators are aligned with their 0.5- × 2-cm unmasked areas spaced by 2.5 cm. A PbS Se diode laser beam is double passed transverse to the molecular beam for an effective path of
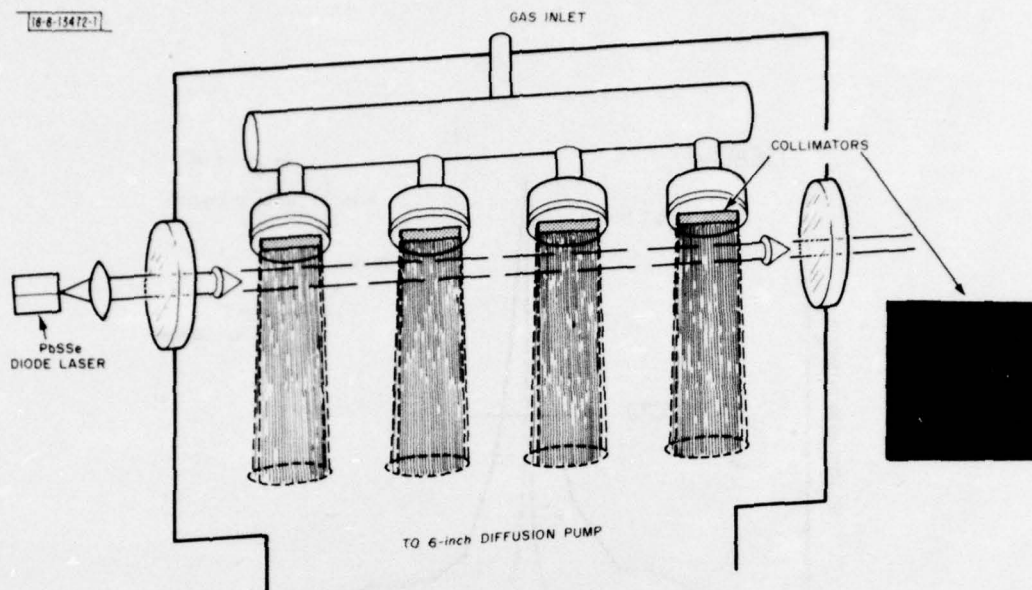
Fig. II-5. Schematic diagram of molecular beam apparatus.

16 cm. The laser is weakly focused ($\lesssim f/50$) inside the chamber about 0.5 cm below the colli-
mators to conform to the molecular beam dimensions. The multitube gas collimators are
glass capillary arrays, obtained from Galileo Electro-Optics Corporation, and are shown mag-
nified in the inset of Fig. II-5. The individual pores are 5 μm in diameter and 2 mm long; the
open active area in the honeycomb is ~40 percent of the total area. The capillary array is
manufactured by repetitively drawing and fusing a packed bundle of glass-cladded glass-core
fibers and etching out the special core after cutting, polishing, and masking the blank to the
desired dimensions. These large-area arrays are necessary to give an intense enough molec-
ular beam to produce measurable absorption. A driving pressure of from 0.1 to 1 Torr is
used behind the collimators and a fast 6-in. diffusion pump below maintains a low background
pressure of less than 10^{-4} Torr.

As depicted in Fig. II-5, the collimation of the molecular shower is not perfect; this fact
is chiefly responsible for the present experimental limit to the Doppler reduction. Figure II-6
shows the actual angular distribution of a helium beam measured in this apparatus using a
collimated collector at the input to a helium leak detector. A portion of the spread shown here
is contributed by the angular resolution of the collector, which is a tube of 0.5 mm inner diam-
eter, 1.3 cm long, pivoted at a radius of 3.5 cm from the collimator; the divergence shown here
agrees roughly with the residual Doppler-width observed spectrally. The theoretical beam angu-
lar distribution is also plotted under the assumption of effusive, resistive (Knudsen) flow and no
interaction between beams from adjacent capillaries. The angular half-width is given theoret-
ically[8] by $\Theta_{FWHM} \simeq 10 \, \delta \sqrt{n_0 r^2/\ell}$ where δ is the kinetic collision diameter of the molecule,
n_0 is driving intensity, and r and ℓ are the radius and length of the capillary. We are more
than an order-of-magnitude broader than this ideal collimator.

Figure II-7 shows derivative spectra of the $R(15/2)_{1/2}$ Λ-doublet in NO obtained by frequency-
modulating the diode laser at 8 kHz as it is scanned. The upper trace is the Doppler-limited

18-8-13474-1

He BEAM P_0 1 Torr

$\Delta\theta \sim 108\sqrt{n_0 r^2/\ell}$

$\sim 1°$

COLLIMATOR

COLLECTOR
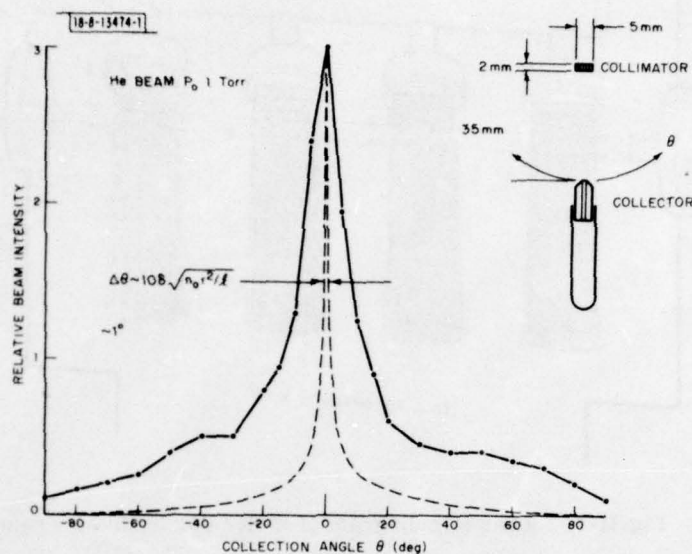
Fig. II-6. Angular distribution of helium beam from capillary array.

18-8-13756

CELL

40 mTorr X 40 cm

X 1

BEAM

0.5 Torr X 16 cm

X 20

FSR = 299.8 MHz
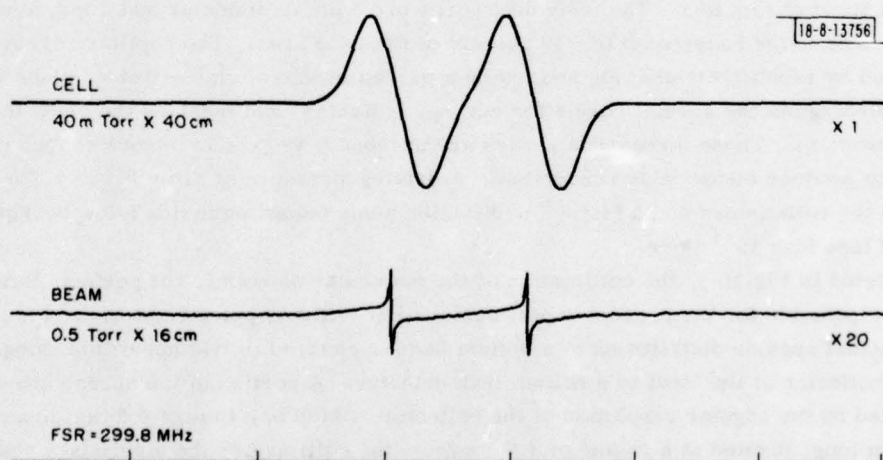
Fig. II-7. Derivative spectra of the $R(15/2)_{1/2}$ Λ-doublet in NO.

22

spectrum taken with a static 40-cm cell with 40 m Torr NO exhibiting the well-resolved Λ-doublet characteristic of the $^2\pi_{1/2}$ states. The lower trace is the same transition obtained with the molecular beam apparatus at an inlet gas pressure of 0.5 Torr behind the nozzles. The pronounced narrowing of the lines indicates a factor of ~20 reduction of the Doppler-broadening due to beam collimation. The frequency scan calibration at the bottom is derived from a semi-confocal interferometer with a free-spectral-range of ~300 MHz. We employ derivative techniques to enhance the signal/noise ratio of the spectra since the absorption is very weak, ≤ 0.1 percent, and rides on a somewhat noisy baseline. We have not found it necessary to use high-frequency Stark modulation of the molecular beam to further discriminate against laser noise, as did Chu and Oka.[8] The sharp structure is somewhat distorted by a broad background arising presumably from the wings of the angular beam distribution shown in Fig. II-6. This broad background is not due to residual backpressure in the vacuum chamber since it disappears when the molecular beam is displaced from the laser beam.

18-8-13757

CELL

40 m Torr X 40 cm   X 1

BEAM

0.5 Torr X 16 cm   X 25

FSR = 299.8 MHz
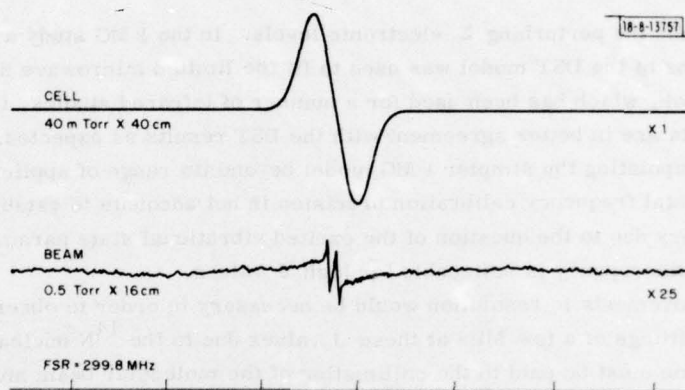
Fig. II-8.   Derivative spectra of the $R(15/2)_{3/2}$ Λ-doublet in NO.

Figure II-8 shows a set of similar traces taken for the $R(15/2)_{3/2}$ Λ-doublet of NO. Here the Λ-doublet is unresolved in the static cell, but is completely resolved in the molecular beam.

Measurements of the Λ-doublet splittings in the $^2\pi_{3/2}$ and $^2\pi_{1/2}$ electronic levels as a function of the combined angular momentum J for high J values accessible in the infrared spectrum of NO provide a good test for the theory of Λ-doubling in the intermediate coupling regime between Hund's cases (a) and (b). This regime is characterized by the rotational transition energies ($2BJ$ with $B \sim 2$ cm^{-1}) being comparable to the spin-orbit splitting ($A \sim 122$ cm^{-1}) separating the $^2\pi_{1/2}$ levels from the $^2\pi_{3/2}$ levels in the electronic ground state. Dousmanis, Sanders, and Townes[9] (DST) have derived a theory of Λ-doubling for the OH radical applicable to the full range of rotational energies. This theory is displayed in Fig. II-9 using spectroscopic parameters appropriate to NO. The Λ-doubling and rotational parameters for NO have been measured on pure rotational transitions for low J in the microwave region by Gallagher and Johnson,[10] and Favero, Mirri, and Gordy[11] (FMG). We assume, for the purposes of this calculation, that these same parameters pertain to the excited vibrational level. Thus we are ignoring the vibrational dependence of the rotational constant and the energy shift between the excited
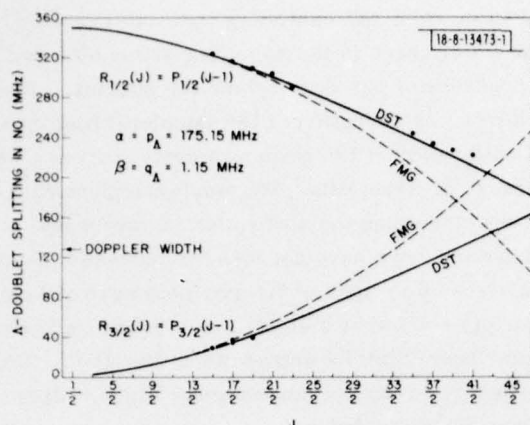
Fig. II-9. Experimental and theoretical J-dependence of Λ-doubling in NO.

vibrational level and the perturbing Σ electronic levels. In the FMG study a power series expansion to J^3 terms of the DST model was used to fit the limited microwave data. A plot of the FMG expression, which has been used for a number of infrared studies, is also shown in Fig. II-9. The data are in better agreement with the DST results as expected, which illustrates the hazard of extrapolating the simpler FMG model beyond its range of applicability. At present, the experimental frequency calibration precision is not adequate to establish any deviation from the DST theory due to the question of the excited vibrational state parameters, though some systematic discrepancy is noticeable for high J values.

Further improvements in resolution would be necessary in order to observe hyperfine structure with splittings of a few MHz at these J values due to the ^{14}N nuclear spin coupling. Here more attention must be paid to the collimation of the molecular beam and the frequency and amplitude stability of the laser. It should be mentioned that the multitube collimators fabricated and tested by others have given angular distributions to within a factor of two of the theoretical; this would yield a tremendous gain in resolution and signal/noise for infrared absorption measurements.

A. S. Pine
K. W. Nill*

C. GAS LASERS OPTICALLY PUMPED BY DOUBLED CO_2 RADIATION

We have previously reported optically pumped laser action in a number of molecules (OCS, CO_2, N_2O, C_2H_2, CS_2, and SiH_4).[12-15] In each case, the molecules were pumped by resonant vibrational energy transfer from CO gas excited by a frequency-doubled CO_2 laser. As reported, higher second-harmonic energies have recently become available.[16] This has improved the performance of the CO_2 laser and the OCS laser significantly. The new results are listed in Table I together with our earlier results on other gases. The maximum output energies from the two lasers are 13 and 5.2 mJ, respectively. The measured maximum slope energy efficiency of 34 percent for CO-CO_2 is close to the maximum possible energy efficiency of 45 percent, which corresponds to unit quantum efficiency. By contrast, even after considerable efforts at optimization, the OCS laser shows a lower efficiency which we believe is due to a bottleneck at the lower laser level. For the direct-pumped OCS laser at 10 Torr,

---

*Laser Analytics, Incorporated, Lexington, Massachusetts 0247 .

TABLE I

SUMMARY OF PERFORMANCE OF OPTICALLY PUMPED LASERS

System	Maximum Pressure (Torr)*	Minimum Threshold		Maximum Efficiency (percent)	Maximum Output (mJ)
		Focused (mJ)	Unfocused (mJ)		
OCS (direct-pumped)	55	0.1	0.6	19.0	5.2
CO-OCS	420	0.1	1.0	7.6	1.3
$CO-CO_2$	12,400 (16.3 atm)	–	1.6	34.0	13.0
$CO-C_2H_2$	610	–	2.0	3.5	0.12
$CO-CS_2$ (11.5 μm)	20	–	2.5	0.5	0.03
CS_2 (6.6 μm)	25	–	6.3	0.1	0.03
$CO-SiH_4$	35	1.7	–	0.6	0.03

*With H_2 or He buffer.

the laser pulse terminates within 500 nsec of the initiation of pumping, well before collisional deactivation of the upper laser level, which takes 2 μsec at 10 Torr (Ref. 17). We believe the reduced efficiency is due to the fact that the lower level deactivation time is long compared to the 200-nsec pulse length. The deactivation rate for OCS has not been measured. On the basis of energy level considerations, however, it is expected to be slower than the comparable rate in N_2O. For N_2O, the deactivation time is 5 μsec at 10 Torr (Ref. 18). Consequently, the maximum efficiency for the direct-pumped OCS laser should be half of unit quantum efficiency. The observed energy efficiency of 19 percent is in reasonable agreement with a theoretical energy efficiency of 29 percent for a quantum efficiency of 0.5.

Previously we have reported laser action on the CS_2 $00^01 \rightarrow 10^00$ transition at 11.5 μm using vibrational energy transfer from CO to pump the 00^01 level. Here we report laser action on the CS_2 $10^01 \rightarrow 10^00$ transition at 6.6 μm using direct optical pumping. The second harmonic of the 9.2-μm CO_2 R(30) line, which lies within 0.041 cm^{-1} of the CS_2 $00^00 \rightarrow 10^01$ P(60) transition,[19] was used for excitation. A similar scheme has recently been demonstrated for CO_2 (Ref. 20). We observed only a single line, the P(60) line, and not the corresponding R(58) line. We tried unsuccessfully to obtain more lines by adding argon, which should promote rotational equilibration without contributing significantly to the deactivation rate of the 10^01 level. The measured threshold energy of 6.3 mJ in Table I was obtained for a 54-cm-long internal mirror cell operated at room temperature with 8 Torr of CS_2. The mirrors were a 1-percent output coupler and a gold total reflector. The laser pulse length varied from 140 nsec at 1.5 Torr to less than

25

(a)

(b)

|← 100 nsec
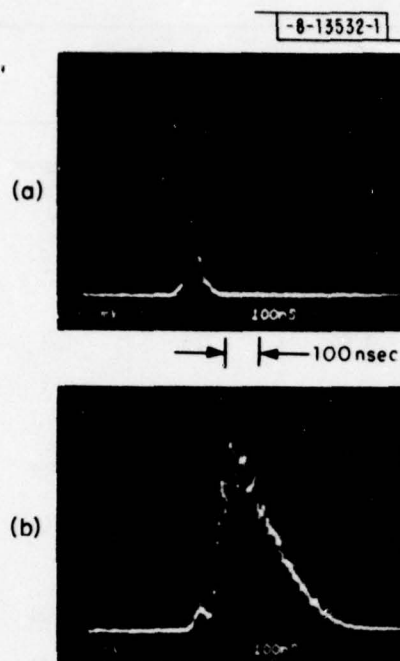
Fig. II-10. Laser output at 6.6 μm from the direct-pumped CS_2 laser using a 54-cm-long laser cell and pressures of (a) 10 Torr, and (b) 1.7 Torr. The small shoulder before the main pulse in Fig. II-10(b) is part of the CO_2 pump pulse.

10 nsec at the high-pressure limit of 25 Torr. At this high-pressure limit, the laser pulse terminated before the pump pulse. Figure II-10 shows the output pulse at CS_2 pressures of 1.7 and 10 Torr.

H. Kildal
T. F. Deutsch

D. HBr-PUMPED 16-μm CO_2 LASER

1. Introduction and Summary

The main emphasis in this effort during the last six months has been to demonstrate unequivocally that this laser is a practical 16-μm source for the ERDA laser isotope separation program.

We summarize our most important results as follows:

(a) In order to demonstrate that the 16-μm laser can be made stepwise tunable, we have achieved laser action in the $^{13}C^{16}O_2$ isotopic species.

(b) The threshold for the 9.6-μm stimulating pulse has been measured to be ~3 mJ. This indicates that a rather large but conventional sealed-off Q-switched laser would be sufficient for driving an isotopic 16-μm laser.

(c) The 16-μm laser pulse energy has been scaled to 120 μJ.

(d) Kinetic measurements of the relaxation of the 16-μm lower level indicate that its relaxation time is of the order of 10^{-5} sec at typical pressures. As a result, high repetition rate operation of the laser is possible.

26

2. Detailed Discussion

a. Isotopic Laser

To achieve limited tunability of the 16-μm laser, it would be desirable to achieve laser oscillation in various CO_2 isotopes. Superficially, it might seem that extension of our 16-μm techniques to other CO_2 isotopes would be trivial, since the isotopic shift among the various species is generally small. However, as we have discussed earlier, relaxation among the Fermi mixed levels of CO_2 is a particularly important physical constraint of our laser. Since the isotopic shift is not small compared to the Fermi interaction energy, collisional rates involving these mixed levels may vary significantly from isotope to isotope.

We have shown that this effect is not significant by demonstrating that 16 μm could be obtained in a relatively common isotope, $^{13}C^{16}O_2$. Again for the purposes of better experimental control, it is preferable to use an external "9-μm" stimulating pulse. The data by Freed et al.[21] indicated that there is a fortuitous near coincidence ($\sim$300 MHz) between P(28) line of $^{12}C^{16}O_2$ and the P(34) line of $^{13}C^{16}O_2$; therefore, a $^{12}C^{16}O_2$ TEA laser was used to provide the stimulating pulse. By using this stimulating wavelength and a high-Q 16-μm cavity we were able to achieve laser action at 16 μm.

b. Measurement of Required 9.6-μm Pulse Energy

The 9.6-μm stimulating pulse power or energy is an important design parameter in this laser. Its magnitude determines whether or not one can efficiently use an internally generated pulse to stimulate the 16-μm laser. In addition, if it is necessary to use both an isotopic CO_2 laser and an externally generated pulse, the magnitude of the pulse energy determines whether one can use a sealed-off Q-switched laser or instead, rely on a TEA laser for the 9-μm source.

Before measuring the pulse energy, it was necessary to narrow the linewidth of the CO_2 TEA laser with a low-pressure gain cell. The pulse power requirement is decreased by the factor $\Delta \nu_P / \Delta \nu_L$, where $\Delta \nu_P$ is the power-broadened gas linewidth in the low-pressure laser cell and $\Delta \nu_L$ is the pressure-broadened TEA laser linewidth. In our case, this factor is approximately 1/10 so that a considerable advantage is obtained with the gain tube in the cavity. The measurement was performed at standard optimal operating condition, i.e., 30 percent output coupling, $-80°C$ gas temperature, 6 Torr 50-50 CO_2-HBr mixture, and a 20-cm sample cell. A Tachisto laser with a $\sim$75-cm gain tube supplied the stimulating pulse.

The result was that approximately 3 mJ of energy in 100 nsec were necessary to extract a significant (i.e., 1/3 of the maximum) 16-μm energy from the laser. This energy is within range of that obtainable from a rather large but conventional sealed-off Q-switched CO_2 laser.

c. 16-μm Energy Optimization

A considerable effort has been made to improve the output energy of the 16-μm laser. We shall only briefly summarize the experimental details here. Improvements have been made as a result of the following changes: increase in cavity output coupling, increase in sample cell length, and improvements in the stimulating laser. A summary of the details of the best experimental run is provided in Table II. The 120-μJ figure quoted there was repeatable on several occasions, and thus was not a one-shot maximum. Perhaps another factor of 1.5 improvement can be realized as a result of further optimization of the laser optics. This factor does not include the improvement to be gained from eliminating the 50-percent loss at 16 μm in the output coupling mirror.

TABLE II

SUMMARY OF EXPERIMENTAL CONDITIONS FOR 16-μm ENERGY OPTIMIZATION

Sample Cell Length	20 cm
Output Coupling	30 percent
Output Mirror Loss at 16 μm	~50 percent
Gas Pressure	2 Torr CO_2 2 Torr HBr
HBr Laser Energy Absorbed	20 mJ
CO_2 Pulse Energy* and Width	400 mJ, 100 nsec
16-μm Energy	120 μJ

* Most energy is lost since no attempt to focus or mode match. No gain tube is in the laser.
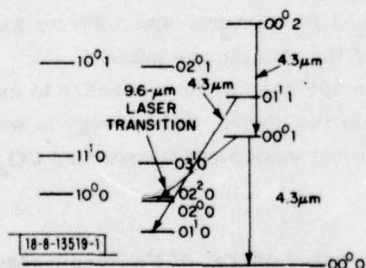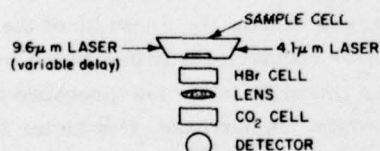
Fig. II-11. The upper figure shows the experimental apparatus used to measure the CO_2 bending mode kinetics. The lower figure gives the various laser and spontaneous transitions which are important to the measurement process. By varying the pressure in the CO_2 filter cell, one can isolate the fluorescence band $01^11 - 01^10$.
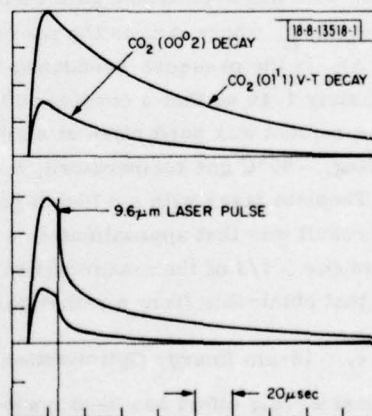
Fig. II-12. Both drawings are traces of oscilloscope photographs of the 4.3-μm fluorescence emanating from the sample cell. The upper drawing shows the decay with no stimulating pulse.

28

d. Kinetics Measurements

The optimization in output power described above has occurred chiefly as the result of a general laser engineering. A deeper understanding of the physical processes occurring in the lasers will allow improvements of a more specific nature. As mentioned above, the fundamental limitation on the laser performance is the relaxation of the Fermi mixed $(00^01-02^00)_{II}$ level. In order to examine the collisional dynamics of this level and, in fact, of the bending mode manifold in general, we have begun measurements on the laser-induced fluorescence from an HBr-CO_2 mixture.

The experimental apparatus for these measurements is shown in Fig. II-11. By varying the gas pressure in the CO_2 filter, the fluorescence from the $01^11 \rightarrow 01^10$ band could be isolated. For the initial experiments, the V-V equilibration between the various CO_2 vibrational modes occurs on an effectively instantaneous time scale. As a result,

$$n(01^11) \approx \frac{n(00^01)\, n(01^10)}{n(00^00)}$$

where n represents the population of the designated CO_2 vibrational mode. Thus the decay in the $n(01^11)$ fluorescence measures the temporal behavior of both the (00^01) and the (01^10) mode populations.

Now if a 9.6-μm stimulating pulse is applied to the mixture after the 4.1-μm excitation pulse, a fluorescence waveform similar to that shown in Fig. II-12 will result. The decay which occurs after the stimulating pulse is a product of the V-T decay of the remaining 00^01 population and of the newly produced, nonthermal 01^10 population. The 01^10 population decays to its thermal value at a rate much faster than the 00^01 population; thus the long time decay measures the slow deactivation of the 00^01 level. As a result, we can measure the deactivation rates of both the 00^01 and 01^10 modes. In fact, the 00^01 decay rate has already been measured previously by Stephenson et al.[22] Our results are reasonable agreement with this rate. However, the deactivation rate of the bending mode by HBr and other hydrogen halides has not been measured. Figure II-13 gives the results of our measurements. Note that this decay rate constant is a factor of 10^2 larger than that of the 00^01 level also by HBr. This unusually fast rate is undoubtedly the result of vibrational-to-rotational deactivation.

MEASURED DECAY RATE FOR
$CO_2(01^10) + HBr \rightarrow CO_2(00^00) + HBr$
IS 6×10^4 S^{-1} TORR^{-1}

18-8-13520-1

DECAY RATE IN 10^5 S^{-1}

HBr PRESSURE IN TORR

Fig. II-13. Experimental data of the decay rate of CO_2 bending mode vs HBr pressure.
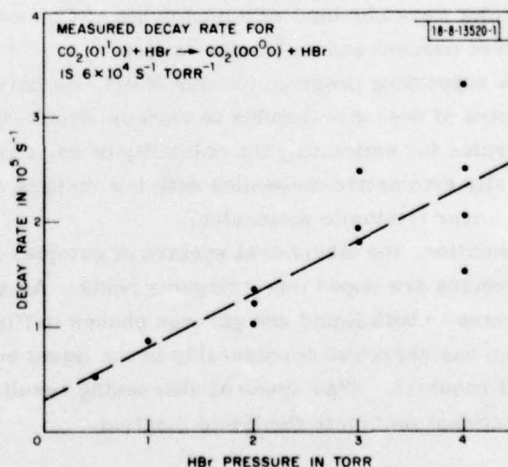
This value of the 01^10 deactivation rate has two implications for the design of a 16-μm laser. First, while fast, the rate is still one to two orders of magnitude slower than the rotational equilibration time. As discussed in Ref. 23, this means that within certain limitations V-R de-activation of the 01^10 is not important during the 16-μm pulse. Further, since the deactivation process $CO([001, 02^00]_{II} + HBr \rightarrow CO_2(01^10) + HBr$ certainly occurs on a comparable time scale, deactivation of the $[001, 02^00]_{II}$ level to the 01^10 level on is also not important (i.e., limiting) process for our laser.

Second, because the deactivation rate is of order 10^4 sec^{-1} at typical operating pressures, it is possible to pulse the same volume of gas at repetition rates up to 10^4 Hz. Thus, for ERDA applications the repetition rate of the present 16-μm laser is limited purely by the pulse rate of the HBr laser. Straightforward engineering improvements in gas flow rates and in the power handling capabilities of the electrical pulses will raise the HBr pulse rate to the 10^3-Hz level.

Finally, present plans are to use laser-induced fluorescence to measure the V-V deactivation rates of the two Fermi levels $[10^01, 02^00]_I$ and $[10^00, 02^00]_{II}$.

R. M. Osgood, Jr.

E. QUANTUM ELECTRONICS OF CRYOGENIC LIQUIDS

Our experimental work has progressed along three avenues: (1) measurement of the vibrational kinetics of molecules in liquid solutions, (2) observation of laser-induced photochemistry in several liquid hosts, and (3) measurement of the infrared spectra of various dopant molecules.

Our measurements of vibration kinetics have been principally with liquid N_2-CO-OCS mixtures in which we have measured the vibrational exchange rates between N_2-CO, CO-OCS, and N_2-OCS. This first rate is particularly interesting because its measurement allows, for the first time, a comparison of the vibrational relaxation processes in both the liquid and gas (previously measured) phases at identical temperatures. The results also give guidance as to the particular mixture one should use to make a liquid-phase OCS laser.

Preliminary laser-induced photochemistry experiments in various liquid hosts have been carried out. We have photolyzed OCS and C_2H_4 in liquid Ar and N_2 with the ultraviolet radiation from CO_2 laser induced breakdown produced in the liquid solvent. In both cases, we could monitor both the disappearance of the parent molecule and the accompanying emergence of the photolytic product (CO or C_2H_2, respectively) by observing the infrared spectrum of the liquid. Similar results were obtained with photolysis of O_2, and the subsequent formation of ozone from reaction of nascent and molecular oxygen.

In a supporting program for our effort, we have attempted to catalog both the solubility and the spectra of dopant molecules in various liquid hosts. As a result, we have developed empirical rules for estimating the solubility of various molecules in each host. For example, spherically symmetric molecules with low melting points have better solubility in liquid nitrogen than do linear triatomic molecules.

In addition, the vibrational spectra of complex molecules is simplified dramatically when the molecules are doped into cryogenic hosts. As an example, we show a comparison of the SF_6 spectra in both liquid and gaseous phases in Fig. II-14. The relatively broad gas phase spectrum has narrowed considerably in the liquid environment, and the sulphur isotope splittings are well resolved. This spectral sharpening results from the elimination of hot bands and of free rotational motion in the liquid medium.

S. R. J. Brueck
R. M. Osgood, Jr.

Fig. II-14. Infrared absorption spectrum of the ν_3 band of SF_6 at room temperature (top) and dissolved in liquid nitrogen at 77 K (bottom). In both cases the SF_6 density is 2×10^{15} cm^{-3} and the path length 6 cm.
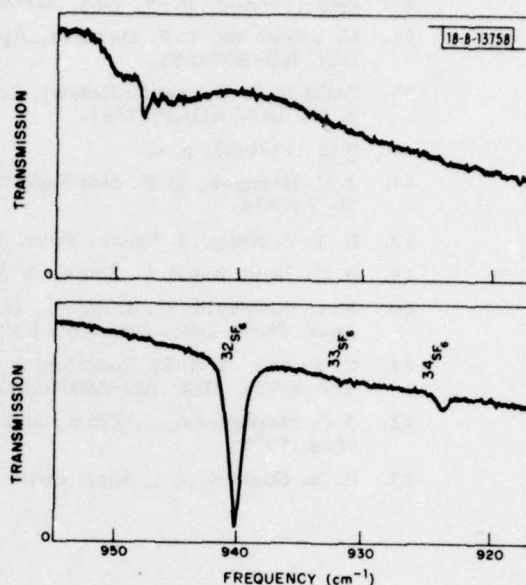
REFERENCES

1. H. Y-P. Hong and K. Dwight, Mat. Res. Bull. 9, 775 (1974), DDC AD-786294/9.

2. G. Huber, W. W. Krühler, W. Bludau, and H. G. Danielmeyer, J. Appl. Phys. 46, 3580 (1975).

3. S. Singh, D. C. Miller, J. R. Potopowicz, and L. K. Shick, J. Appl. Phys. 46, 1191 (1975).

4. K. Otsuka, T. Yamada, M. Saruwatari, and T. Kimura, IEEE J. Quantum Electron. QE-11, 330 (1975).

5. K. Dwight, private communication.

6. S. R. Chinn and H. Y-P. Hong, Opt. Commun. 15, 345 (1975), DDC AD-A024235.

7. C. K. N. Patel, Appl. Phys. Lett. 25, 112 (1974).

8. F. Y. Chu and T. Oka, J. Appl. Phys. 46, 1204 (1974).

9. G. C. Dousmanis, T. M. Sanders and C. H. Townes, Phys. Rev. 100, 1735 (1955).

10. J. J. Gallagher and C. M. Johnson, Phys. Rev. 103, 1727 (1956).

11. P. G. Favero, A. M. Mirri and W. Gordy, Phys. Rev. 114, 1534 (1959).

12. Solid State Research Report, Lincoln Laboratory, M.I.T. (1974:4), p. 33, DDC AD-A004763/9.

13. Ibid (1975:3), p. 24, DDC AD-A019472/0.

14. H. Kildal and T. F. Deutsch, Appl. Phys. Lett. 27, 500 (1975), DDC AD-A024185.

15. Solid State Research Report, Lincoln Laboratory, M.I.T. (1976:1), p. 37, DDC AD-A027261.

16. Ibid (1976:2), p. 17.

17. J. K. Hancock, D. F. Starr and W. H. Green, J. Chem. Phys. 61, 3017 (1974).

18. R. T. V. Kung, J. Chem. Phys. 63, 5305 (1975).

19. A. G. Maki and R. L. Sams, J. Mol. Spectrosc. 52, 233 (1974).

20. M. I. Buchwald, C. R. Jones, H. R. Fetterman, and H. R. Schlossberg, Appl. Phys. Lett. (to be published).

21. C. Freed, A. H. M. Ross and R. G. O'Donnell, J. Mol. Spectrosc. 49, 439 (1974), DDC AD-A000518/1.

22. J. C. Stephenson, J. Finzi, and C. B. Moore, J. Chem. Phys. 56, 5214 (1971).

23. R. M. Osgood, Jr., Appl. Phys. Lett. 28, 342 (1976).

III. MATERIALS RESEARCH

A. INTERACTION OF ADSORBED WATER MOLECULES WITH SURFACE DEFECTS ON TiO_2

In the photoelectrolysis cells so far investigated, surface states of the oxygen electrode are believed to play an essential role in the photocatalytic decomposition of water into H_2 and O_2 (Ref. 1). We have previously described the formation and nature of defect surface states on TiO_2 (rutile),[2] the material that has been most widely employed as an oxygen electrode for photo-electrolysis. We have now begun to study the interaction of adsorbed H_2O molecules with these surface defects. Studies of this type, conducted with monolayer amounts of adsorbed H_2O in ultrahigh vacuum, are a first step toward understanding the catalytic activity of electrode materials.

We have used ultraviolet photoemission spectroscopy to investigate the effects of adsorbed H_2O on the TiO_2 surface states and the changes produced in the H_2O molecules on adsorption. Photoemission spectra using He I radiation (21.2 eV) were taken first for a clean surface and then for the same surface after adsorption of H_2O. The two spectra were digitized by using a Hewlett Packard Model 9830A calculator equipped with a digitizing table, and the difference between them was taken digitally.

Figure III-1(a) shows the photoemission spectra for an annealed TiO_2 (110) surface.[2] The photoemitted electron density n(E) is plotted vs electron initial state energy, measured from the upper edge of the valence band E_v. The solid line is the spectrum for the atomically clean surface, and the dashed line is for the same surface after exposure to 10^8 Langmuirs of H_2O at room temperature. There is a small, residual surface-state peak in the energy gap at -2 eV due to a few surface defects left after annealing.[2] Figure III-1(b) shows the difference between the two spectra in Fig. III-1(a). In Fig. III-1(c), the solid curve is the photoemission spectrum for a clean, heavily Ar-ion-bombarded TiO_2 (110) surface ($\alpha_s > 4$ in the terminology of Ref. 2), and the dashed curve is for the same surface after exposure to 10^8L of H_2O. The peak observed at about -3 eV for the clean surface is the surface-state peak that arises from rearrangement of the surface Ti ions.[2] The difference between the two spectra in Fig. III-1(c) is shown in Fig. III-1(d). Figure III-1(e) is the photoemission spectrum for H_2O in the gas phase.[3]

The most striking effect of the adsorption of H_2O occurs on the high-defect-density surface. The dip at -3 eV in the difference spectrum of Fig. III-1(d) indicates that adsorption causes partial depopulation of the defect surface state. The three peaks at 1.3, 4.3, and 6.9 eV are strongly suggestive of the $1b_1$, $2a_1$ and $1b_2$ orbitals of the gaseous H_2O molecule, respectively. Accordingly, we have lined up the gas-phase photoemission spectrum of H_2O in Fig. III-1(e) with the difference spectrum. The relative positions of the b_1 and b_2 orbitals match exactly with the 1.3- and 6.9-eV peaks. The 4.3-eV peak is shifted $\sim$1 eV towards tighter binding with respect to the a_1 orbital of gaseous H_2O, suggesting that H_2O bonds to the TiO_2 surface defect via its a_1 orbital.

Heavy Ar-ion bombardment of TiO_2 results in the loss of oxygen, producing surface oxygen vacancies. Like the H_2O molecule, these vacancies have C_{2v} symmetry. The surface state associated with such a vacancy [$V_O(C_{2v})$] is an a_1 bonding state (with charge in the vacancy) formed by superposition of Ti (3d) orbitals. Our model for the bonding of H_2O to the bombarded TiO_2 surface assumes that the H_2O molecule is adsorbed at the vacancy site and maintains
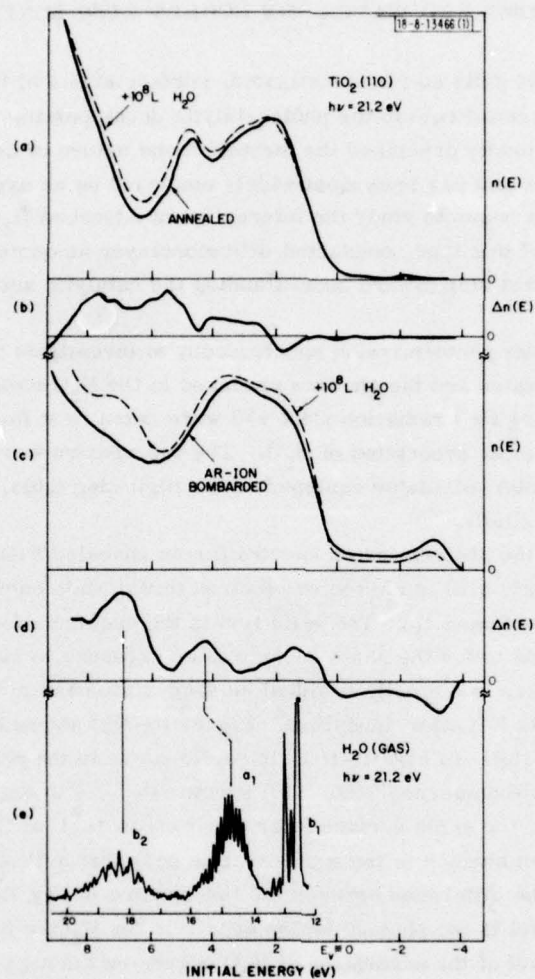
Fig. III-1. Ultraviolet photoemission spectra for (a) annealed TiO$_2$ (110) before (solid curve) and after (dashed curve) exposure to 10^8 L H$_2$O; (b) difference between spectra in (a); (c) Ar-ion-bombarded TiO$_2$ before (solid curve) and after (dashed curve) exposure to 10^8 L H$_2$O; (d) difference between spectra in (c); and (e) photoemission spectrum of gaseous H$_2$O (Ref. 3), shifted to match difference spectrum in (d).

34

C_{2v} symmetry. The a_1 (H_2O) and a_1 [$V_O(C_{2v})$] orbitals strongly interact, repelling each other by about 1 eV. With these shifts, the surface state no longer bonds an electron. The strong bonding to the surface also distorts the H_2O molecule. Due to the concentration of electronic charge in the surface bond, the separation between H^+ ions in H_2O increases, and hence the bonding of an H^+ ion to the H_2O-vacancy complex is greatly decreased.

The difference spectrum in Fig. III-1(b) for the adsorption of H_2O on the nearly defect-free, annealed TiO_2 (110) surface is more complicated than that on the high-defect-density surface. The annealed surface appears to adsorb less H_2O than does the defect surface, and the data suggest that H_2O may bond to two different sites on the annealed surface; a better signal-to-noise ratio in the difference spectrum is necessary before any firm conclusions can be drawn on the latter point, however.

Defect surface states on TiO_2 have been shown to exist in three distinct phases.[2] The energy of the surface states associated with the Ti^{3+}/oxygen-vacancy complexes existing at low defect densities ($\alpha_s \leqslant 1$ in the terminology of Ref. 2) suggests that these defects are the ones that are important in photoelectrolysis. We plan to extend our photoemission studies of H_2O adsorption to this defect regime in order to obtain a better understanding of the surface parameters that are important in photoelectrolysis.

<div align="right">
V. E. Henrich
G. Dresselhaus
H. J. Zeiger
</div>

B. EFFECT OF CESIATION ON THE WORK FUNCTION OF CdTe

The demonstration of transferred-electron photoemission from InP (Ref. 4) has spurred interest in developing transferred-electron photocathodes using other crystal systems, including a graded $Hg_xCd_{1-x}Te$ structure proposed previously.[5] In the latter system the photoemissive surface would be CdTe, so efficient operation would require lowering the potential barrier at the CdTe-vacuum interface below the bottom of the bulk CdTe conduction band. In principle, this might be done either by biasing a Schottky barrier formed by depositing a thin metal layer on the CdTe surface, the procedure followed for InP (Ref. 4), or by cesiating the CdTe surface to a state of negative electron affinity (NEA). The second alternative is very attractive because the resulting photodiode would be a two-terminal device not requiring biasing of the photoemissive surface. Since the cesiation of CdTe has not been reported, we have begun an investigation of the interaction of Cs and O_2 with CdTe to determine whether an NEA surface can be produced. In initial experiments, we have been able to obtain a reduction of 2.4 eV in the work function of both n- and p-type CdTe by a series of alternate exposures to Cs and O.

The CdTe samples studied were cut from two single crystals, one n-type (Ga-doped, 3×10^{17} electrons/cm^3), the other p-type (Cu-doped, $\sim 2 \times 10^{16}$ holes/cm^3). The n-type samples were rods with a [110] axis, so excellent (110) surfaces could be obtained by cleaving in the ultrahigh vacuum system. The p-type samples were (111) wafers that were first lapped and chemically etched, then placed in the vacuum system and Ar-ion sputter-etched. The activation procedure consisted of alternate Cs and O exposures at room temperature, always beginning with Cs. The Cs source used for most of the activations was a Cs-ion gun in which Cs is produced by thermal decomposition of a Cs-zeolite; similar results were obtained with a Cs thermal channel.[6] In each Cs activation step using the Cs-ion gun, the surface was bombarded with about 5×10^{15} Cs ions/cm^2 at an ion energy of about 20 eV. In each O_2 activation step the surface was exposed to 300 L of O_2. After each activation step, the work function was determined from the low-energy

cutoff of an ultraviolet photoemission spectrum taken with He I radiation ($h\nu \approx 21.2$ eV). The photoemission spectra contain a wealth of band-structure and surface-state information, some of which is discussed below.

Both n- and p-type CdTe surfaces behaved in essentially the same manner during activation, and there was also very little difference between cleaved and sputter-etched surfaces. Figure III-2 shows photoemission spectra taken at three points during the activation of a p-type CdTe wafer. The ordinate $n(E)$ gives the relative number of photoemitted electrons per energy interval, and the abscissa is the initial-state energy measured from the Fermi level. (The position of the Fermi level is determined independently from the photoemission spectrum of a gold sample.) While the initial-state energy of electrons increases to the left in Fig. III-2, their kinetic energy in vacuum increases to the right. The sharp drop in photoemitted intensity at the left end of each trace thus determines the position of the vacuum level (i.e., electrons with
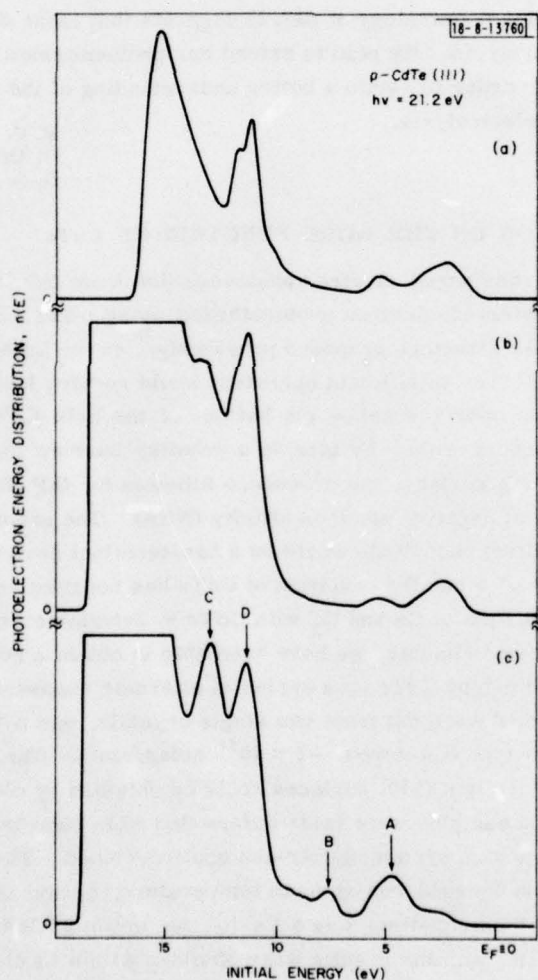
Fig. III-2. Ultraviolet photoemission spectra, $n(E)$, vs initial state energy measured from the Fermi level, for p-CdTe (111) during activation. (a) Atomically clean; (b) after one Cs exposure; and (c) after four Cs and three O_2 exposures.

lower kinetic energy cannot escape from the sample). The band-structure features in Fig. III-2 are superimposed on a background of inelastically scattered photoelectrons that exhibit a peak just above the vacuum level; in Figs. III-2(b) and -2(c) this peak is about ten times off scale and has been clipped.

Figure III-2(a) is the spectrum for atomically clean CdTe. The Fermi level lies about 0.5 eV above the top edge of the uppermost valence band. This valence band, which yields the two-peaked structure between 0.5 and 6.0 eV, is composed mainly of Cd(5s) and Te(5p) electrons. A lower-lying valence band, consisting of the Cd(4d) and Te(5s) electrons, gives the structure between 9.5 and 12.5 eV. The work function of this clean CdTe surface, determined from the location of the photoemission cutoff, is about 4.7 eV. Figure III-2(b) is the spectrum taken after one Cs exposure. The work function has dropped to 2.6 eV, and the total photoemitted flux is about ten times that from the clean surface. There is presumably no more than one monolayer of Cs on the surface, but we have no measure of the actual coverage. The structure of the lower valence band is somewhat distorted, and a new peak has appeared at about 13 eV. Figure III-2(c) is a spectrum taken after four Cs and three O_2 exposures, the number of steps that gives the lowest work function (2.3 eV) and highest photoemitted flux that we have obtained. The upper valence-band structure is very different from that of the clean surface, with two new peaks (A and B) appearing. The lower valence-band structure between 10 and 15 eV is dominated by two peaks (C and D).

In Fig. III-3 the work function φ and the heights of peaks A, B, and C are plotted for the clean CdTe surface and after each Cs or O_2 exposure. Adjacent data points are connected by

Fig. III-3. (a) Work function and (b) height of peaks A, B, and C after each step of the activation procedure of p-CdTe (111).
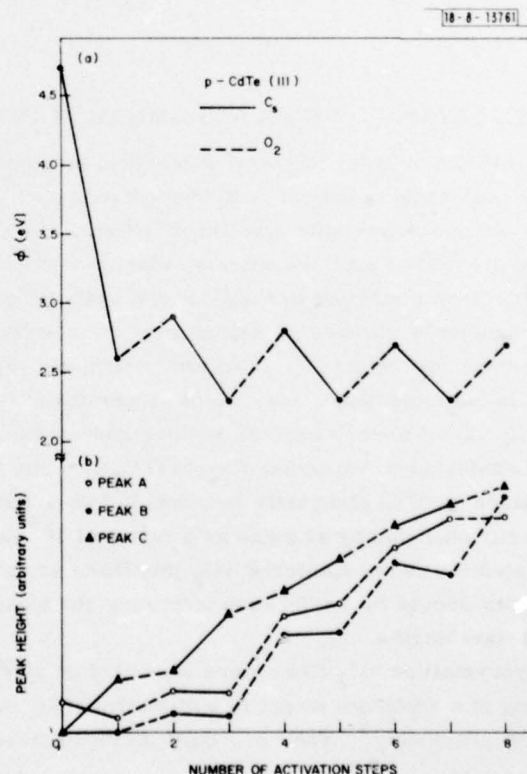
solid lines for Cs exposures and dashed lines for O_2 exposures. The work function [Fig. III-3(a)] drops by 2.1 eV after the first Cs exposure, then rises by 0.3 eV on exposure to O_2. The second Cs exposure drops the work function 0.3 eV below its value after the first Cs exposure. Similar behavior is observed during activation of III-V photocathodes.[7] Several Cs-O_2 cycles are necessary to obtain maximum photoresponse. In this type of activation, each O_2 step raises the work function, so the final step is always a Cs exposure. From several activations of both n- and p-type CdTe, we find that four Cs exposures give the lowest work function.

The heights of peaks A, B, and C during activation are shown in Fig. III-3(b). Peak B exhibits a particularly striking behavior, increasing only after O_2 exposures and staying relatively constant during Cs steps. It therefore is almost certainly due to emission from an oxygen band, and its location (7.6 eV) agrees with the value of 7.1 ± 0.8 eV for the O(2p) band given by Bearden and Burr.[8] Peak A is probably also due to an oxygen band since it exhibits a similar dependence during the first six steps; it has a different behavior for the last two steps, however. Peak C shows the inverse behavior during the first three activation steps, increasing after the Cs exposures and remaining fairly constant during the O_2 exposures. Beginning with the fourth step, however, it rises smoothly. Its location (13.0 eV) and that of peak D (11.3 eV) are very close to the values of 13.1 ± 0.5 and 11.4 ± 0.5 eV for the Cs($5p_{1/2}$) and Cs($5p_{3/2}$) levels given in Ref. 8.

While the results reported here are encouraging, it is not yet clear whether NEA can be achieved on CdTe. The details of the work-function and band-structure changes during each activation step are being studied in order to optimize the procedure, and the effect of different crystallographic orientations is being investigated. Experiments are also planned with more highly p-type CdTe, since NEA can only be achieved if the Fermi level is pinned in the valence band.

<div align="right">

V. E. Henrich
D. L. Spears
A. J. Strauss

</div>

C. APPLICATIONS OF INSULATOR-METAL TRANSITIONS

A preliminary study has been undertaken to assess the potential of insulator-metal transitions for utilization in optical switching devices such as modulators and switchable diffraction gratings for use as variable-wavelength filters. Over 20 compounds of the transition and rare-earth metals exhibit such transitions, which are characterized by an abrupt change in electrical properties from insulating to metallic at a well-defined transition temperature. The transition is accompanied by changes in optical properties which are greatest in the infrared region where free-electron absorption effects dominate when the material is in the metallic state. The large changes in their electrical and optical properties at the phase transition make these compounds potentially useful for applications in microelectronics and optoelectronics. In this work, we have concentrated on vanadium dioxide (VO_2), partly because it has a convenient transition temperature (~65°C) and partly because it has a fairly large transition, with the electrical conductivity changing by as much as a factor of 10^5 in single crystals. In particular, we have investigated the use of sputtered VO_2 thin films as optical switches at submillimeter wavelengths. The results should be useful in determining the feasibility of this class of devices at near-infrared wavelengths.

Polycrystalline VO_2 films were deposited on single-crystal sapphire substrates by reactive sputtering of a vanadium target in a mixture of Ar and O_2. The growth conditions have been described previously.[9] They are quite critical because preparation of films with desired

properties is made difficult by the existence of many different compounds in the vanadium-oxygen system.[10] For the best films, the resistivity changes by a factor of about 2×10^3 at 65°C.

For transmission experiments, submillimeter radiation provided either by an HCN laser at 337 μm or by optically pumped molecular lasers was measured with a GaAs photoconductive detector. In initial experiments, we determined the change in transmission at 337 μm that occurred when a VO_2 film 2500 Å thick, deposited on a sapphire substrate 0.6 mm thick, was heated through the phase transition with an external heater. With the film in the insulating state, the transmission of the film-substrate composite was close to 80 percent, the same within the experimental uncertainty of 5 percent as the transmission of the bare substrate. Transition to the metallic state reduced the transmission to only 25 percent, a relative decrease of about 70 percent.

In view of the rather large change in optical transmission observed in the initial tests, a series of experiments was performed to explore the modulating properties of devices in which the VO_2 film is heated through the transition temperature by passing an electric current through it. The configuration used, which was fabricated by means of photoresist masking and photolithographic techniques, is shown schematically in Fig. III-4. It consists essentially of four
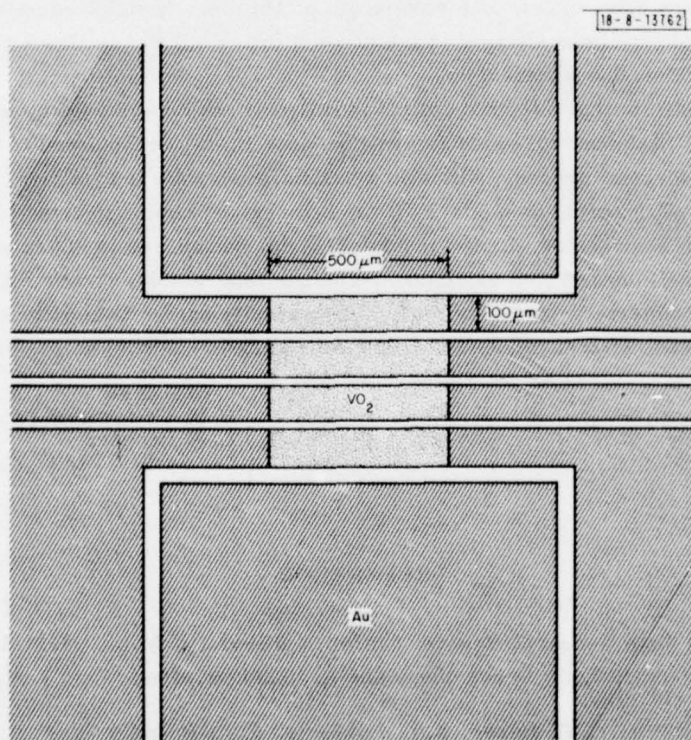

Fig. III-4. Schematic diagram of optical modulator consisting of four VO_2 elements.

rectangular VO_2 elements, each 100×500 μm, with gold contacts at the ends. To prepare this structure, a film of VO_2 2500 Å thick was deposited on a sapphire substrate, and the four elements were defined by removing unwanted VO_2 with 1:1 HNO_3:H_2O_2 etchant. Films of titanium 500 Å thick (to provide adhesion between the VO_2 and gold) and gold 3000 Å thick were deposited on the substrate by RF sputtering, after which the unwanted gold and titanium were successively removed by etching first with an iodine-based etchant and then with 20:1 H_2O:HF. The narrow stripes between the VO_2 elements, where the bare substrate was exposed for electrical isolation, were blocked by depositing gold on the reverse side of the substrate in order to minimize light leakage. The electrical resistance of each element was about 50 kΩ at room temperature, and the resistance changed by more than a factor of 10^2 at the phase transition.

To obtain optical modulation, an electronic pulse generator was used to apply trains of 160-V pulses to the VO_2 elements, causing their temperature to increase and decrease periodically as the current was switched on and off. The degree of modulation, defined in terms of the maximum and minimum transmission observed, was measured as a function of pulse repetition frequency. The pulse duty cycle was adjusted for maximum modulation at each frequency. At a frequency of 100 Hz, laser radiation at 337 μm was modulated by approximately 70 percent, about the same percentage obtained in the experiments with an external heater. When the frequency was increased to 1000 and 2000 Hz, however, the modulation decreased to 60 and 50 percent, respectively. This decrease resulted because the cooling rate was insufficient for the entire film to return to the insulating state during the times when the current was not flowing, even though the substrate was mounted on a water-cooled platform. Similar results were obtained in preliminary experiments at a wavelength of 151 μm. Modulation should also occur at 10 μm, but this could not be confirmed in the present experiments because sapphire is not sufficiently transparent at this wavelength.

Our results indicate that effective optical modulation can be achieved by utilizing insulator-metal transitions. Modulation frequencies will be quite limited for materials like VO_2 in which the transition is a thermal process, although speeds significantly higher than those obtained here with water cooling should be achieved if the devices are cooled to cryogenic temperatures. However, it has been suggested that the insulator-metal transitions in materials like Cr-doped V_2O_3 are Mott transitions, driven by electron-electron interactions rather than thermal excitation.[11] If such materials can be switched electronically rather than thermally between the insulating and metallic states, much faster optical modulators should be possible.

J. C. C. Fan   P. M. Zavracky
H. R. Fetterman   C. D. Parker
F. J. Bachner

REFERENCES

1. Solid State Research Report, Lincoln Laboratory, M.I.T. (1976:2), p. 33.

2. V. E. Henrich, G. Dresselhaus and H. J. Zeiger, Phys. Rev. Lett. 36, 1335 (1976).

3. D. W. Turner, C. Baker, A. D. Baker and C. R. Brundle, Molecular Photoelectron Spectroscopy (Interscience, New York, 1970).

4. R. L. Bell, L. W. James and R. L. Moon, Appl. Phys. Lett. 25, 645 (1974).

5. I. Melngailis, "The Graded-Gap Semiconductor Photoemitter," Technical Note 1971-8, Lincoln Laboratory, M.I.T. (22 January 1971), DDC AD-720796.

6. Provided by A. H. Sommer of Thermo Electron Corp.

7. A. H. Sommer, personal communication.

8. J. A. Bearden and A. F. Burr, Rev. Mod. Phys. 39, 125 (1967).

9. J. C. C. Fan and F. J. Bachner, Solid State Research Report, Lincoln Laboratory, M.I.T. (1972:3), p. 39, DDC AD-752556.

10. K. Kosuge, J. Phys. Chem. Solids 28, 1613 (1967); J. B. MacChesney, J. F. Potter and H. J. Guggenheim, J. Electrochem. Soc. 115, 82 (1968).

11. D. B. McWhan, T. M. Rice and J. P. Remeika, Phys. Rev. Lett. 23, 1384 (1969); D. B. McWhan and J. P. Remeika, Phys. Rev. B2, 3734 (1970).

IV. MICROELECTRONICS

A. CHARGE-COUPLED DEVICES: PROCESSING

Considerable attention has been given to the problem of improving yields in our CCD processing. Wafers of 30- × 30-cell prototype imaging arrays have recently been fabricated with improved processing techniques, and have exhibited yields of over 90 percent when tested for diode leakage and gate-to-gate and gate-to-substrate shorts. Dynamic testing of these devices will result in a somewhat lower yield, but the results of static testing are very encouraging.

As described in a previous report,[1] our goal is to develop for the GEODSS (Ground Electro-Optical Deep Space Surveillance) Program a hybrid sensor consisting of 16 CCD imaging arrays, each having 100 × 400 or 40,000 resolution elements. The chip size of 70,000 mils[2] is comparable in size to the largest state-of-the-art integrated circuits. To obtain any acceptable devices requires careful processing, with much attention to wafer cleanliness at all critical steps in the process. Prior failures in this regard have resulted in a major yield problem on some wafers caused by a very high occurrence of shorts, either between the two levels of polysilicon gates or between the gates and the substrate.

Several sources of contamination in the fabrication process have been identified as contributors to this problem, and steps have been taken to reduce them as much as possible. Cleaning of wafers is a critical step and is carefully monitored by inspecting wafers under bright and dark field illumination under a microscope. Cleaning and etching operations often leave or fail to remove significant levels of particulates on silicon wafers, particularly in the case of sulfuric acid which is used after photoresist stripping. The use of plasma stripping of photoresist as an alternative to sulfuric acid has resulted in considerably lower contamination levels.

To monitor the effectiveness of new fabrication procedures, several wafers of 30- × 30-cell prototype imaging arrays have been processed. This device is similar to one described previously,[1] but has been redesigned for improved performance. An indication of the expected yield of good 100 × 400 devices can be obtained from yield data on the smaller but otherwise identical 30 × 30 device using simple models for yield versus active device area.[2] These models suggest that yields of about 90 percent on the 30 × 30 device will be required in order to expect a yield of one good 100 × 400 device from a wafer of 28. Recently completed runs of the 30 × 30 device have shown yields of well over 90 percent when tested for diode leakage, gate-to-gate, and gate-to-substrate shorts. While we expect the final yield to be somewhat lower after the devices undergo complete dynamic testing, the results of the static testing are highly encouraging.

<div style="text-align: right">

B. E. Burke
R. A. Cohen
R. W. Mountain

</div>

B. CHARGED-COUPLED DEVICES: DYNAMIC TESTING

Several of the 30 × 30 devices discussed in the previous section have been dynamically tested using an electrical input signal. The capability of inserting signals electrically is a useful addition to a CCD imaging device and costs little in terms of added device area. Electrical inputs are simpler and more effective than optical inputs for setting optimum clocking voltages and for measuring charge transfer efficiency. Transfer efficiencies of 0.9998 or greater have been measured for the output registers of several devices, and the transfer efficiency of a single complete device has been determined to be equivalently high.
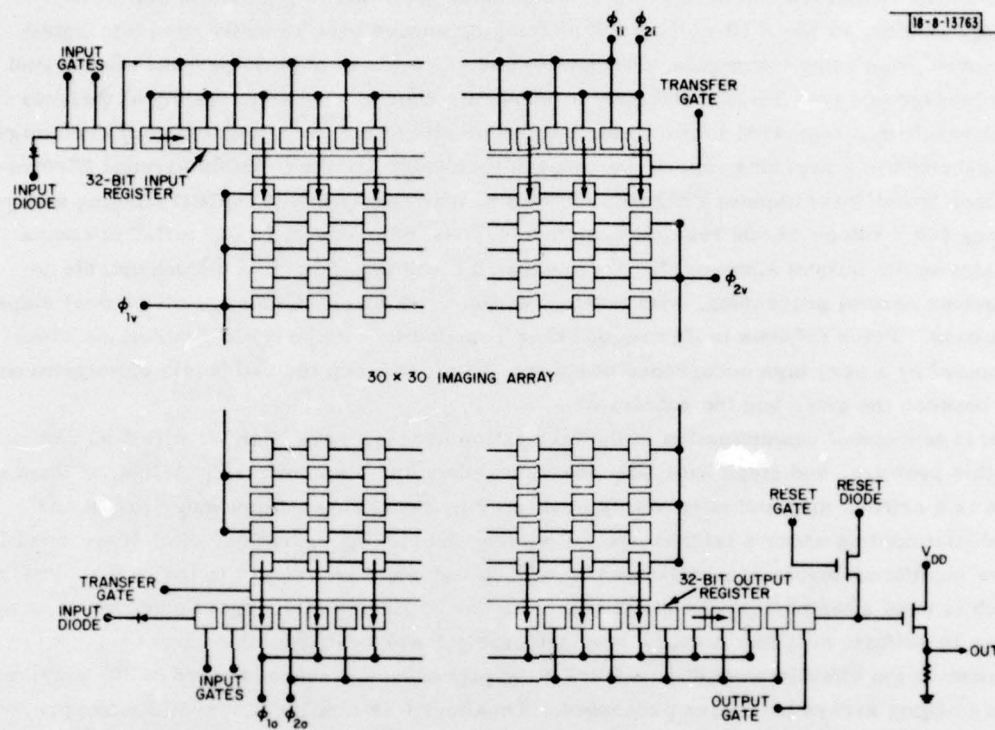
Fig. IV-1. Schematic of the prototype CCD consisting of 2-phase 32-bit input and output registers and a 30 × 30 imaging array. The device functions either as a serial-parallel-serial analog delay line by use of an electrical input to the input register, or as a simple 32-bit serial device by use of an electrical input to the output register.

A schematic diagram of the device is shown in Fig. IV-1. It is designed with a serial-parallel-serial (SPS) format, and is capable of storing 900 analog signal samples. A 32-bit input register (at the top of Fig. IV-1) is used to clock 30 charge packets to the right until they are aligned with the 30 columns of the imaging array. At this point, a transfer gate, normally biased to a negative potential to prevent charge flow into the array, is momentarily pulsed "on," permitting transfer of the charge packets from the input register, across the transfer gate, and into the first row of cells in the imaging array. The transfer gate is then turned "off," and another set of 30 charge packets is clocked into the input register while the packets in the imaging array are transferred down by one row. Simultaneously, a similar but reverse situation is occurring at the 30th row of the imaging array where a second transfer gate admits successive rows of 30 charge packets into 30 cells of a 32-bit output register. These charge packets are then transferred to the detection circuitry at the output. An additional feature of this device is an electrical input to the output register permitting this part of the device to be characterized.

Transfer efficiencies measured using only the output registers of the 30 × 30 devices have been greater than 0.9998 per transfer on all devices tested. Measurements on the full device operating as an SPS register are somewhat more complicated in that the amplitudes of several clocking waveforms must be adjusted if optimum transfer efficiency is to be achieved. Operation of the device as an SPS register is illustrated in Fig. IV-2(a-c). The top waveform in each case is a signal applied to an input gate of the input register and consists of consecutive pulses, each timed to insert 30 equal charge packets into the input register. (The last pulse actually delivers 31 charge packets due to imprecise control over the timing of the input signal pulse generator for high duty-rate pulse bursts.) The bottom waveform shows the output signal resulting from an identical set of consecutive pulses applied 1.2 msec earlier. The charge packets are clocked into and out of the registers at an 800-kHz rate. The output consists of sets of 30 pulses separated by 4 clock periods. The first two clock periods are used to allow charge flow across the transfer gates, and the latter two represent the delay in traversing the last two cells of the output register.

Examples of how non-optimum device operation is diagnosed are shown in Figs. IV-2(a) and (b). In Fig. IV-2(a), the upper transfer gate is adjusted to allow only partial charge transfer into the imaging array. The charge left in the input register is then clocked further to the right and accumulated in the last cells until they are overfilled. This results in large amplitude signals from the columns at the right side of the device. Improper biasing of the lower transfer gate results in the signal shown in Fig. IV-2(b). Here the charge transfer is not complete, and charge which is left in the bottom row of the imaging array is partially transferred to the output register at later times. Satisfactory operation of a device is shown in Fig. IV-2(c), where a high degree of uniformity in output pulse amplitude is evidence of a high transfer efficiency in each part of the device. The slight nonuniformities can be attributed at least in part to the input signal pulses, which deviate slightly from an ideal flat top, and to a small level shift of the output MOSFET. In addition, the fifth signal in each group is enhanced by a small amount of dark current from that column. However, from detailed analysis we can conclude that the transfer efficiency for the device as a whole is greater than 0.9998.

B. E. Burke
W. H. McGonagle
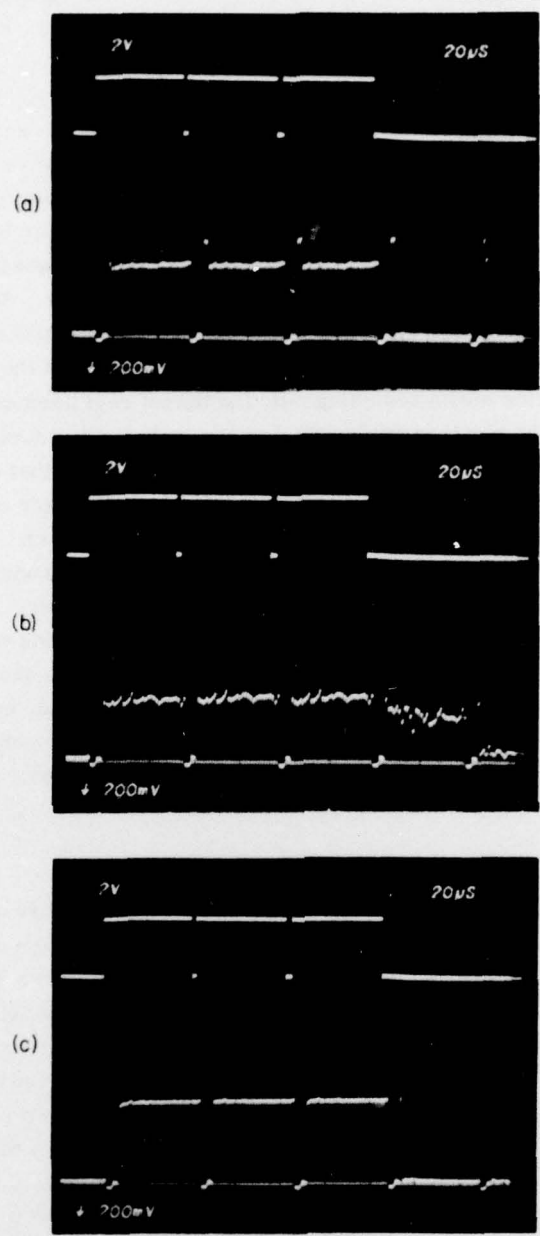
Fig. IV-2. Oscilloscope photographs showing serial-parallel-serial operation of a device. Upper trace is the input signal which causes 3 sets of 30 charge packets to be clocked into the input register. Lower trace is the delayed output showing: (a) improper biasing of top transfer gates; (b) improper biasing of lower transfer gates leading to poor charge transfer efficiency; (c) all clocking levels are optimized, and the overall transfer efficiency exceeds 0.9998 per transfer.

C. IMPURITY GETTERING IN SEMI-INSULATING GALLIUM ARSENIDE USING ION IMPLANTATION DAMAGE

Gettering of impurities from semi-insulating gallium arsenide has been achieved using neon- and silicon-ion-implantation damage with a subsequent 16-hour anneal at 750°C. The amount of gettering was determined by an evaluation of epitaxial layers grown on the gettered samples after removal of the damaged material. Impurity profiles of layers grown on these surfaces show a dramatic reduction in the out-diffusion of compensating impurities from the substrate into the epitaxial layer.

Although considerable work has been done with ion-implantation-damage gettering in silicon,[3,4] none has been reported for gallium arsenide. It is possible that this ion-implantation-damage gettering will be useful in providing better substrates for application to gallium arsenide microwave FETs. In addition, because the gettering effects occur in the temperature range for epitaxial growth and ion-implantation anneals, this gettering phenomena could also be important in understanding and improving growth and annealing procedures.

The two ions which were separately evaluated for their ability to produce damage gettering were Ne^+ and Si^+. Neon was chosen because it should remain neutral in the crystal and have no effect on the gettering other than the damage it created, whereas silicon could be chemically active in the crystal and for this reason have some additional gettering properties. The wafers of semi-insulating gallium arsenide used in these experiments all came from a single ingot which had a resistivity of 1.3×10^8 ohm-cm. The wafers were chem-mechanically polished on one side and chemically etched on both sides to remove mechanical damage. The implants were made into the polished face at room temeprature with a dose of $10^{16} cm^{-2}$ Ne^+ at 400 keV for one wafer, and $10^{16} cm^{-2}$ Si^+ at 400 keV for a second wafer. The depth of damage is estimated to be 1 μm for Ne^+ and 0.6 μm for Si^+.[5,6] These samples were then overcoated with Si_3N_4 on the polished face, and additionally with SiO_2 front and back as described previously.[7,8] Both wafers were annealed at 750°C for 16 hours in flowing nitrogen. After anneal, the silicon dioxide layer was removed with hydrofluoric acid, and the silicon nitride was removed by reactive ion etching using a mixture of 5% O_2 in CF_4. The plasma etch was found to be necessary for nitride removal because the standard wet chemical techniques left a film of relatively inert material on the surface of the wafer which interfered with subsequent chemical-etch steps. After nitride removal, the samples were soaked for 5 minutes in 47% hydrochloric acid.

Immediately prior to epitaxial growth, all the wafers were etched in room-temperature $5:1:1$ $H_2SO_4:H_2O_2:H_2O$ for one minute to remove the ion-implantation-damaged layer. The etch also removes an n-type layer under the damaged layer which forms during the anneal to a depth of about 3 μm. After the procedure just described, the wafer still has its pre-implanted surface smoothness and its high resistivity. The epitaxial system was of the $Ga-AsCl_3-H_2$ type, and the growth temperature was 740°C.[9] The epitaxial layer was grown simultaneously on the Ne^+ and Si^+ damaged wafers and also on a control wafer from the same crystal which had not been ion damaged. There was no in-situ vapor etch used in the epitaxial growth sequence. The initial 2 μm of epitaxial growth was intentionally doped to 2.5×10^{16} cm^{-3} with sulfur in order to provide a low-resistance back contact for the C-V technique used to measure the impurity profiles. The rest of the 16-μm-thick epitaxial layer was grown with no intentional doping. The growth rate was held constant at 8 μm/hr, and the total growth time was 2 hours.

The impurity profiles for the three epitaxial layers are given in Fig. IV-3. The electron concentration in the epitaxial layer on the control sample decreases with distance from the
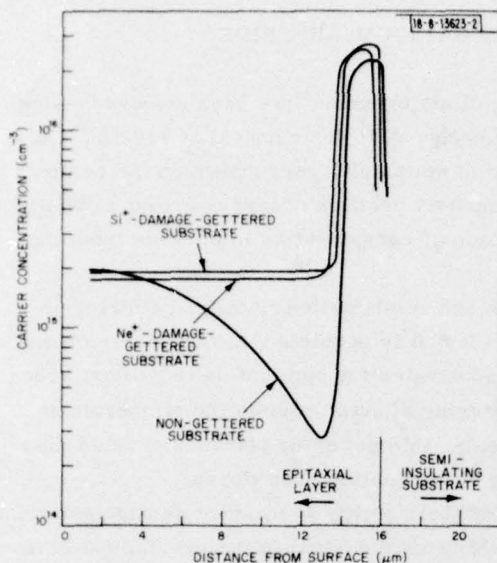
Fig. IV-3. A comparison of epitaxial layers grown on gettered and non-gettered semi-insulating GaAs substrates. The initial 2 μm of all the layers was intentionally doped with sulfur to 2.5×10^{16} cm^{-3} in order to provide a low-resistance back contact for the C-V measurement. The final 14 μm of the layer was not intentionally doped.

surface, whereas the profiles for the two ion-implantation-damaged wafers are flat. We believe that the decrease in concentration in the control layer is due to the outdiffusion of compensating impurities or defects from the substrate, and that these impurities or defects are gettered by ion-implantation damage and a subsequent anneal. The conclusion is supported by experiments where epitaxial layers were grown simultaneously on Cr-doped semi-insulating and silicon-doped n$^+$ substrates with growth conditions similar to those just described. The profiles of the layers on the semi-insulating substrates were similar to that of the control sample of Fig. IV-3, and the profiles of the layers on the n$^+$ substrates had flat profiles similar to those on the ion-damaged substrates. Because of the simultaneous growth, the difference in the two profiles could not be caused by autodoping and must be caused by a difference in the two substrates. In addition, layers grown for longer times on semi-insulating substrates had a thicker compensated region. The time dependence could only be explained by impurities or defects diffusing out of the substrate. This outdiffusion effect was observed for substrates from many ingots of semi-insulating gallium arsenide from various manufacturers, but has never been observed for n$^+$ substrates.

To be sure that the gettering was due to the damage and not the silicon nitride, an epitaxial layer was grown on a substrate with no ion-implantation damage which was encapsulated, annealed, and etched as described above. The profile of this layer showed a small reduction of outdiffusion when compared to a simultaneously grown layer on a control wafer, thus indicating some gettering. The reduction in outdiffusion, however, was not nearly as great as that shown in Fig. IV-3.

These results indicate that the concentration of fast diffusing impurities found in semi-insulating GaAs can be greatly reduced, at least in the neighborhood of the damaged surface, by using ion-implantation-damage gettering. Since both Ne$^+$ and Si$^+$ damage had the same gettering effect, it is very likely that damage is the gettering agent rather than any chemical activity of the ions.

C. O. Bozler
J. P. Donnelly
W. T. Lindley

REFERENCES

1. Solid State Research Report, Lincoln Laboratory, M. I. T. (1975:4), pp. 45-46, DDC AD-A025489.

2. B. T. Murphy, Proc. IEEE 52, 1537 (1964).

3. T. E. Seidel and R. L. Meek, in Proceedings of the Third International Conference on Ion Implantation in Semiconductors and other Materials, 1973, p. 305.

4. C. M. Hsieh, J. R. Mathews, H. D. Seidel, Appl. Phys. Lett. 22, 238 (1973).

5. J. Lindhard, M. Scherff, H. Schiott, K. Dan Videvsk, Selsk. Mat.-Fys. Medd 33, 1 (1963).

6. J. F. Gibbons, W. S. Johnson and S. W. Mytroie, Projected Range Statistics, 2nd Ed. (Dowden, Hutchinson & Ross, Inc., 1975).

7. J. P. Donnelly, W. T. Lindley and C. E. Hurwitz, Appl. Phys. Lett. 27, 41 (1975), DDC AD-A016690/0.

8. C. O. Bozler, J. P. Donnelly, R. A. Murphy, R. W. Laton, R. W. Sudbury, and W. T. Lindley, Appl. Phys. Lett. 29, 123 (1976).

9. C. O. Bozler, Solid State Research Report, Lincoln Laboratory, M. I. T. (1975:2), p. 52, DDC AD-A013103/7.

V. SURFACE-WAVE TECHNOLOGY

A. X-RAY LITHOGRAPHY USING Cu_L RADIATION

Most x-ray lithographic replication of submicrometer-linewidth patterns has used aluminum sources[1,2] with radiation primarily at a wavelength of 8.3 Å. For replicating patterns with line-widths of the order of 1000 Å, it is preferable to use a softer x-radiation in order to increase the attenuation in the mask absorber pattern and to reduce the range of the randomly directed Auger and photoelectrons that are excited when the exposing x-ray is absorbed. Our work has used the characteristic L radiation (13.3 Å) emitted from a copper target. At this wavelength, the attenuation of gold is 55 dB/μm (as compared to 20 dB/μm at 8.34 Å), and thus the mask absorber pattern need be only 1000 Å thick in order to provide more than 5 dB contrast. If poly-methyl methacrylate (PMMA) is used for recording the pattern, such a mask contrast is more than adequate.

The effective range in PMMA of the Auger and photoelectrons which are excited when a copper-L x-ray is absorbed is of the order of 200 Å, which is accordingly the intrinsic resolution limit of the copper-L x-ray lithography.

In addition to the characteristic L radiation, a copper source also emits a continuous spectrum and a K line at 1.54 Å (if bombarded by electrons with energies above 8 keV). This continuous spectrum can potentially degrade resolution because of the large range of the higher energy photoelectrons excited upon absorption in the resist. However, these harder x-rays are less readily absorbed in the polymer film (resist), and an analysis for a copper source operated at 8 kV shows that the amount of power absorbed from the L line in a 1-μm-thick polymer film exceeds that absorbed from the continuum by a factor of about 20 to 1.

The types of x-ray masks developed for use with aluminum-K x-ray sources are not suitable for use with a copper-L source because of the high attenuation in the mask's membrane (~8 dB at 13.3 Å). Such high attenuation results in long exposure times and decreases the ratio of characteristic-to-continuum absorbed in the polymer. Figure V-1 illustrates the type of x-ray mask used in the copper-L work. The Si_3N_4 and SiO_2 are deposited by a CVD process. The silicon is etched in ethylenediamine pyrocatechol and water at 110°C. The thin aluminum film is an infrared reflector to prevent heating of the polymer film.
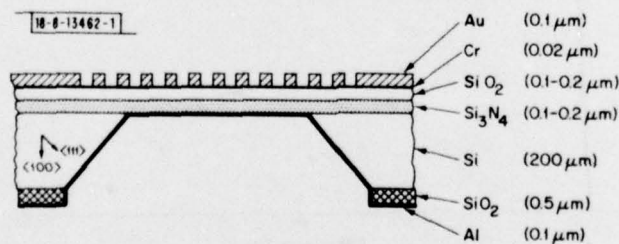

Fig. V-1.   Cross-sectional schematic of an x-ray mask for use with the copper-L radiation (13.3 Å). The Si3N4 and SiO2 layers are grown by a CVD process on a silicon wafer. The aluminum film acts as a reflector to prevent heating of the polymer by in-frared radiated from the source.
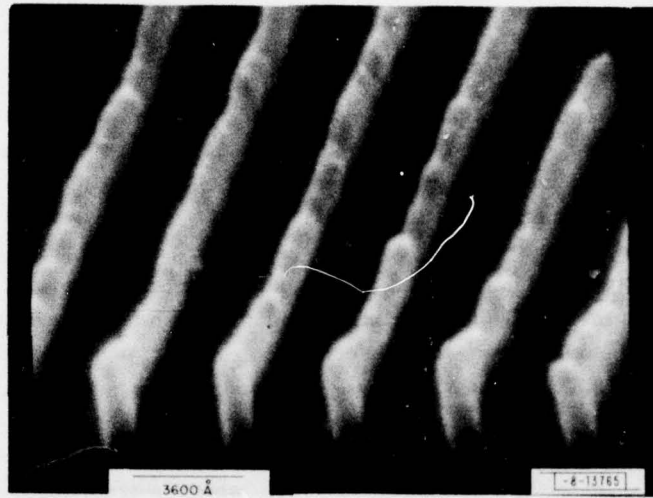
Fig. V-2. Scanning electron micrograph of the cross section of a grating pattern exposed in polymethyl methacrylate using the copper-L x-radiation (13.3 Å).
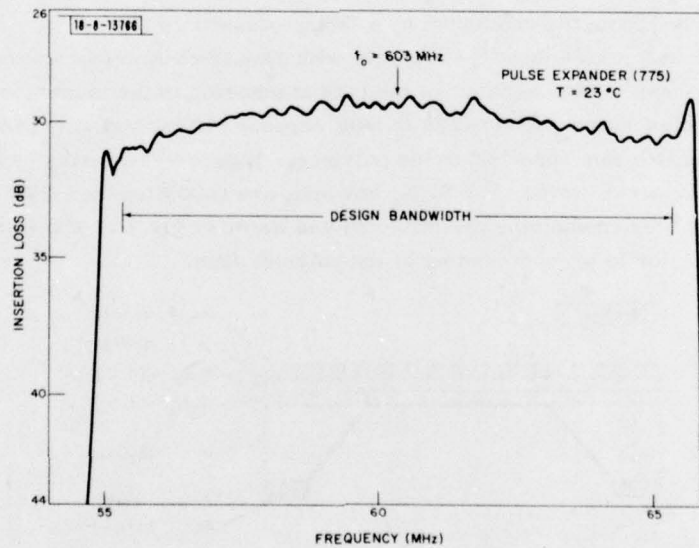

Fig. V-3. Frequency response of 10-MHz-bandwidth reflective-array compressor on bismuth germanium oxide.

Figure V-2 is a scanning electron micrograph of the cross section of a grating pattern exposed in PMMA using the copper-L x-radiation. The grating pattern was produced on the mask by holographic exposure of photoresist over a 1000-Å-thick gold film, followed by ion-beam etching of the gold. The sharp vertical sidewalls and smooth edges illustrate the high resolution capability of x-ray lithography and the absence of significant substrate backscattering.

In order to obtain sharp vertical sidewalls in patterns exposed in polymer film, penumbral effects must be minimized. This is done by holding the x-ray mask in intimate contact with the substrate by electrostatic means. The aluminum-film IR shield serves as the back electrical contact.

<div align="right">D.C. Flanders
H.I. Smith</div>

B. BISMUTH GERMANIUM OXIDE REFLECTIVE-ARRAY COMPRESSORS

Because of the relatively low surface-wave velocity (1681 m/sec) on bismuth germanium oxide, this material is useful for obtaining large dispersion in pulse expanders and compressors. Devices with large linear-FM dispersion and relatively narrow bandwidth (2.5 MHz) have previously been developed for the MASR system.[3,4] In addition, 10-MHz-bandwidth linear-FM devices were developed for MASR and advances in reflective-array technology were required to meet the demands for low insertion loss in the new devices.

In the wideband (10-MHz) mode of operation of the MASR system, it is necessary that the signal to noise in the expanded waveforms be greater than 60 dB. To achieve such a signal-to-noise ratio with a passive pulse expander and with limited (<1 W) peak exciter power, it is necessary that the device have a CW insertion loss less than 30 dB. To achieve this, both transducer conversion loss and grating reflection loss must be minimized.

At the radar IF of 60 MHz, the 10-MHz bandwidth corresponds to a 17-percent fractional bandwidth. This represents a relatively large fractional bandwidth for efficient conversion by interdigital transducers on BGO which has a low electromechanical coupling coefficient, $K^2/2 = 0.0068$. Calculations of transducer response showed that maximum efficiency across the required bandwidth was obtained by adding a pair of phase-reversed fingers to each end of a six-finger-pair transducer. Delay-line measurements showed that the transducers contributed 15 dB of loss at midband with an increase to 17 dB at the band edges. Diffraction and propagation losses contributed an additional 1 to 5 dB across the design bandwidth. Thus, in order to meet the 30-dB insertion-loss goal, the grating reflection loss had to be held to less than 10 dB.

In order to determine the grating depth profiles necessary to achieve overall reflection losses less than 10 dB, it is necessary to employ a reflectivity model which includes the effects of multiple reflections.[5] The pulse-expansion units were depth weighted according to this model to obtain uniform response across the operating bandwidth. However, the measured CW frequency response showed a 3-dB tilt across the band. By adjustment of an inductor in the matching circuit for each transducer, it was possible to tilt the device response and largely compensate for tilts in the grating response thus obtaining an acceptably flat overall response. Figure V-3 shows the frequency response obtained with midband insertion loss at 30 dB and approximately 1 dB gradual fall-off toward the band edges.

The amplitude-weighted frequency response of the matched pulse compressors showed a maximum deviation of approximately 0.5 dB from the desired Hamming-weighted response. Midband insertion loss is 30 dB, the design value.

Phase measurements made on each RAC device show that the chirp slopes of the individual pulse compressors are nearly equal and match the chirp slope of the pulse expander. In each device, the rms phase error was reduced from 20° to approximately 2°. On two of the devices, a double-compensation scheme was successfully used to further reduce phase errors.

A complete waveform-generation and compression subsystem was fabricated for the MASR system. The compact assembly contained a 2.5-MHz-bandwidth expander and matched compressor as well as a 10-MHz-bandwidth expander and three matched pulse compressors.

<div style="text-align: right">

V. S. Dolat
R. C. Williamson

</div>

C. DUAL ACOUSTOELECTRIC CONVOLVER FOR PROCESSING OF DPSK SIGNALS

A dual acoustoelectric convolver has been developed for the ARPA Packet Radio System. This device provides the capability to decode differential-phase-shift-keyed (DPSK) data which have been spread to a 100-MHz bandwidth by means of continuously changing, pseudorandom, bit-encoding waveforms. The bit rate is 100 kbps, corresponding to a spreading factor of 1000. Development of acoustoelectric convolvers was described in a previous Solid State Report.[6] At that time, undesirable temperature variations of device response were encountered. In the current devices, improved packaging techniques provide temperature stability and are compatible with commercial fabrication techniques.

A prototype convolver capable of providing a matched-filter function for a 10-μsec 100-MHz waveform was previously developed for ARPA.[7,8] This device was able to decode 100-kbps, phase-shift-keyed (PSK) data which had been spread to 100-MHz bandwidth by means of pseudonoise, PSK bit-encoding waveforms which changed from bit to bit. However, decoding PSK waveforms requires a coherent local oscillator as reference, which is unavailable in many communication systems. It was therefore decided that the final device to be developed for the Packet Radio System should be able to decode differential-phase-shift-keyed (DPSK) data. In this case, no coherent reference is required, but two adjacent bits must be matched filtered and their relative phases compared. Thus, a differential phase of 180° corresponds to a binary "1," while 0° corresponds to "0."

One means of accomplishing this DPSK decoding process would be to use two 10-μsec convolvers and a 10-μsec delay line to provide matched filtering and alignment of the correlation spikes, respectively. Such a structure would require temperature regulation of the order of tens of millidegrees between the respective acoustic substrates. Even if all components were integrated onto the same substrate for temperature tracking, minute air-gap variations could allow unacceptable changes in the relative phase of the output of the two convolvers.

To eliminate problems of phase variations with temperature, it was decided to use a single convolver device of 20-μsec time capacity. By segmenting the silicon of such a device into 10-μsec elements, a phase comparison of the simultaneous correlation spikes of two adjacent 10-μsec bits could be performed in a sum-difference hybrid. Because all signals propagate along the same acoustic path, inherent temperature stability is achieved. Assembly of such a device required that two 1.375-in. by 0.030-in. strips of silicon be laid end-to-end over a single 0.030-in.-wide acoustic beam path. By means of an indium-bonding technique adapted from work on laser diodes, the two silicon strips are precisely aligned and bonded to a thin (3- to 5-mil) Kapton sheet.
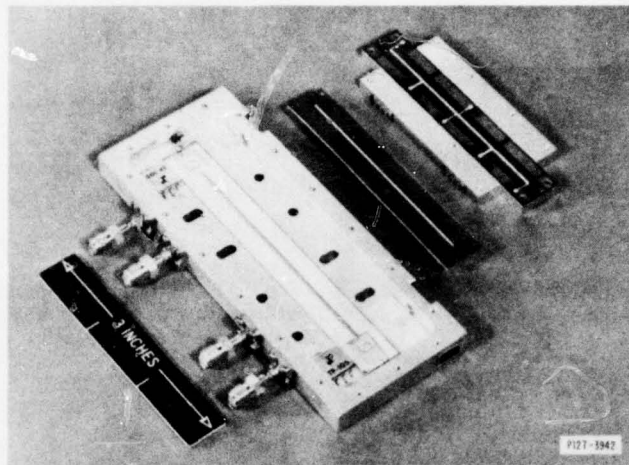
Fig. V-4. Principal dual-convolver subassemblies consisting of a LiNbO₃ crystal and package with the input matching networks, two 30-mil-wide silicon strips bonded end to end on a Kapton sheet, and a plate piece with the electrical output components.

The three principal subassemblies of the convolver are shown in Fig. V-4. A gold-plated aluminum base holds a 0.05- × 0.5- × 4-in. lithium-niobate crystal with transducers and ground planes on it. The area between the ground plane has a pseudorandom array of 5-μm-dia. spacer posts which maintain a uniform airgap of 3500 Å between the silicon and lithium niobate after assembly. At each end, there is an alumina substrate which has an inductor, a quarter-wave stripline, and a 4:1 impedance transformer. These components are required to match the transducers to 50 Ω over the 100-MHz 1-dB bandwidth. The next subassembly is the Kapton sheet with two 1.375-in.-long by 0.030-in.-wide silicon strips indium bonded end to end on it. Finally, a plate piece with a Kapton circuit supplies all terminations and output connections to the silicon.

Figure V-5 shows a partially assembled device, in which the plate piece and silicon are in place. Chip resistors, which terminate the transmission lines formed by the silicon, can be seen through four elongated holes. Four-to-one impedance transformers connect the centers of the silicon strips to the external system. Also shown are the RTV strip, beryllium-copper shim, spring guide, springs, and pressure plate. These items are assembled into the cavity behind the silicon, and act to maintain the desired pressure on the silicon over a wide temperature range.

To improve the temperature performance of the convolvers, extensive testing has been carried out on 10-μsec structures. Initially, the 10-μsec devices showed a 12- to 25-dB variation in convolver efficiency over the temperature range from 0° to +75°C. As a result of improvements in the mechanical package and the spacer-post pattern, our two most recent 10-μsec devices had variations in convolver efficiency of 4 dB and 6 dB, respectively, over the same temperature range. This degree of variation is approximately equal to the theoretically predicted residual variation due to the temperature dependence of carrier mobility in the silicon.

One of the keys to this improvement is the use of beryllium-copper springs which transmit a nearly constant and uniform pressure to the back of the silicon through an intervening layer
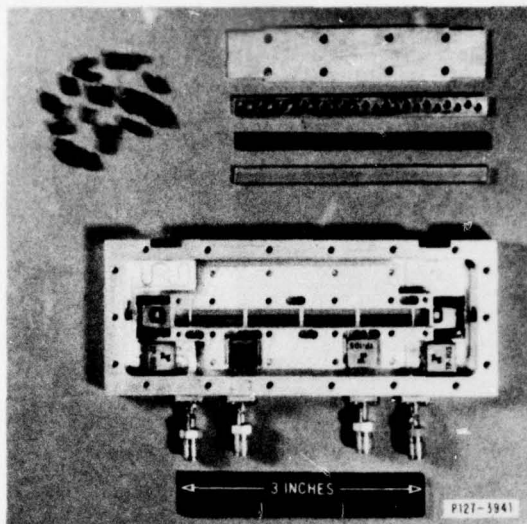
Fig. V-5. Complete convolver assembly
with springs and mechanical components
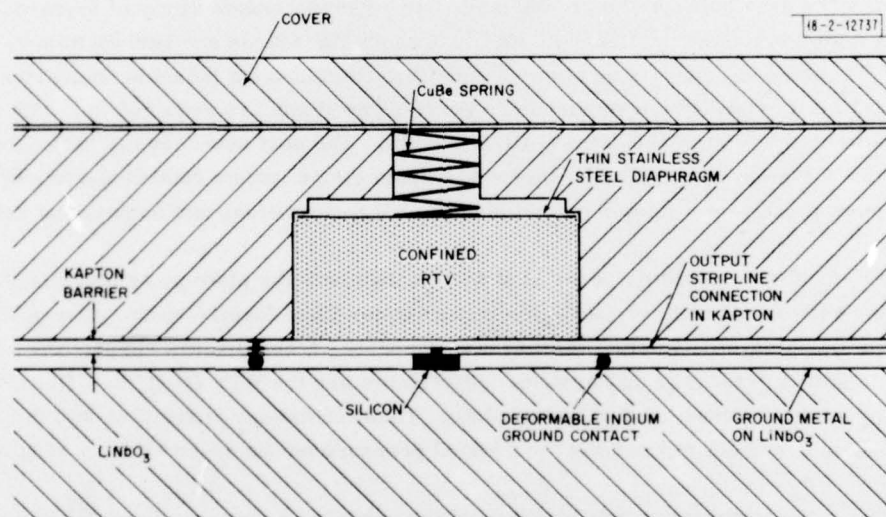which maintain a stable $LiNbO_3$-silicon
air gap.

Fig. V-6. Cross-sectional view of the assembled convolver.
The beryllium-copper springs provide a constant pressure
and compensate for the thermal expansion of the confined
RTV.

of RTV rubber as shown in Fig. V-6. While the expansion coefficient of RTV is nearly an order of magnitude greater than the aluminum package which confines it, the springs have an elastic constant which decreases with temperature. The result is a structure which nearly completely compensates for the thermal expansion of its various components resulting in a very stable air gap.

One of the 10-μsec devices possessing the recent improvements has been cycled 21 times over the temperature range of −25° to +75°C with no apparent degradation in performance. Convolver efficiency was repeatable to within ±0.5 dB over this temperature range. Improvements which were developed as a result of experiments on the 10-μsec convolver have been incorporated in the final design of the dual convolvers.

<div style="text-align:right">

S. A. Reible   R. W. Ralston
J. H. Cafarella   E. Stern

</div>

REFERENCES

1. D. L. Spears, H. I. Smith, and E. Stern, "X-Ray Replication of Scanning Electron Microscope Generated Patterns," Electron and Ion Beam Science and Technology (Fifth International Conference), R. Bakish, Ed. (The Electrochemical Society, Inc., Princeton, New Jersey, 1972), p. 80.

2. R. Feder, E. Spiller, and J. Topalian, "Replication of 0.1-μm Geometries with X-Ray Lithography," J. Vac. Sci. Technol. 12, 1332 (1975).

3. Solid State Research Report, Lincoln Laboratory, M.I.T. (1975:4), pp. 60-62, DDC AD-A025489.

4. V. S. Dolat and R. C. Williamson, "BGO Reflective-Array Compressor (RAC) with 125 μsec of Dispersion," in 1975 Ultrasonics Symposium Proceedings (IEEE, New York, 1975), p. 490.

5. O. W. Otto, "Multiple Reflections in Acoustic Surface Wave Reflective Arrays," IEEE Trans. Sonics Ultrason. SU-22, 251-257 (1975).

6. Solid State Research Report, Lincoln Laboratory, M.I.T. (1976:1), p. 69, DDC AD-A027261.

7. J. H. Cafarella, J. A. Alusow, W. M. Brown, and E. Stern, "Programmable Matched Filtering with Acoustoelectric Convolvers in Spread-Spectrum Systems," in 1975 Ultrasonics Symposium Proceedings (IEEE, New York, 1975), p. 279.

8. J. H. Cafarella, W. M. Brown, E. Stern, and J. A. Alusow, "Acoustoelectric Convolvers for Programmable Matched Filtering in Spread Spectrum Systems," Proc. IEEE 64, 756 (1976).

REPORT DOCUMENTATION PAGE		READ INSTRUCTIONS BEFORE COMPLETING FORM
1. REPORT NUMBER ESD-TR-76-226	2. GOVT ACCESSION NO.	3. RECIPIENT'S CATALOG NUMBER
4. TITLE (and Subtitle) Solid State Research, 1976:3.		5. TYPE OF REPORT & PERIOD COVERED Quarterly Technical Summary rept. 1 May – 31 July 76 6. PERFORMING ORG. REPORT NUMBER 1976:3
7. AUTHOR(s) Alan L. McWhorter		8. CONTRACT OR GRANT NUMBER(s) F19628-76-C-0002
9. PERFORMING ORGANIZATION NAME AND ADDRESS Lincoln Laboratory, M.I.T. P.O. Box 73 Lexington, MA 02173		10. PROGRAM ELEMENT, PROJECT, TASK AREA & WORK UNIT NUMBERS Program Element No. 65705F Project No. 649L
11. CONTROLLING OFFICE NAME AND ADDRESS Air Force Systems Command, USAF Andrews AFB Washington, DC 20331		12. REPORT DATE 15 Aug 76 13. NUMBER OF PAGES 76
14. MONITORING AGENCY NAME & ADDRESS (if different from Controlling Office) Electronic Systems Division Hanscom AFB Bedford, MA 01731		15. SECURITY CLASS. (of this report) Unclassified
		15a. DECLASSIFICATION DOWNGRADING SCHEDULE

16. DISTRIBUTION STATEMENT (of this Report)

Approved for public release; distribution unlimited.

17. DISTRIBUTION STATEMENT (of the abstract entered in Block 20, if different from Report)

18. SUPPLEMENTARY NOTES

None

19. KEY WORDS (Continue on reverse side if necessary and identify by block number)

solid state devices	surface-wave technology	imaging arrays
quantum electronics	photodiode devices	infrared imaging
materials research	lasers	surface-wave transducers
microelectronics	laser spectroscopy	

20. ABSTRACT (Continue on reverse side if necessary and identify by block number)

This report covers in detail the solid state research work of the Solid State Division at Lincoln Laboratory for the period 1 May through 31 July 1976. The topics covered are Solid State Device Research, Quantum Electronics, Materials Research, Microelectronics, and Surface-Wave Technology. Funding is primarily provided by the Air Force, with additional support provided by the Army (BMDATC), ARPA (MSO, IPTO), NSF, and ERDA.

207 650   mt